Construction and Building Materials 292 (2021) 123426

Contents lists available at ScienceDirect

Construction and Building Materials

journal homepage: www.elsevier.com/locate/conbuildmat

Assessment of longitudinal and transversal plastic behavior of recycled aggregate self-compacting concrete: A two-way study

Víctor Revilla-Cuesta [a,1], Marta Skaf [b,1], Amaia Santamaría [c,2], Vanesa Ortega-López [a,*], Juan Manuel Manso [a]

[a] Department of Civil Engineering. University of Burgos, Spain
[b] Department of Construction. University of Burgos, Spain
[c] Department of Mechanical Engineering. University of the Basque Country, UPV/EHU, Spain

HIGHLIGHTS

- 15 SCC subjected to continuously-increasing-load and loading/unloading tests.
- Stress–strain curves in both directions and ratio between their strains obtained.
- Yield step and cracking by vertical splitting highly affected transverse behavior.
- Recycled SCC transverse damaged after cyclic elastic loading of increasing severity.
- Advisable SSC design according to serviceability conditions in compressed elements.

GRAPHICAL ABSTRACT

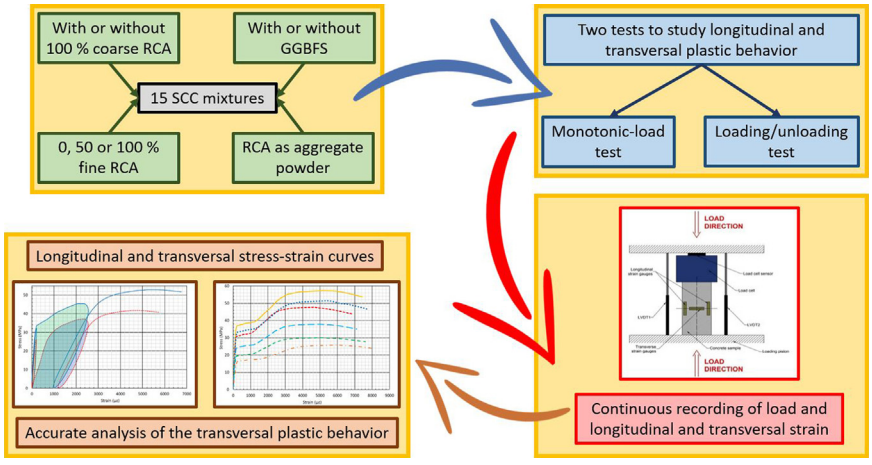

ARTICLE INFO

Article history:
Received 14 January 2021
Received in revised form 5 April 2021
Accepted 17 April 2021
Available online 29 April 2021

Keywords:
Self-Compacting Concrete (SCC)
Recycled Concrete Aggregate (RCA)
Plastic behavior
Stress–strain curves
Longitudinal and transversal strain
Loading/unloading test

ABSTRACT

Plastic strain behavior in the transversal direction to the axis of loading has often been underestimated in concrete design and its strength performance. However, as this article demonstrates, it is fundamental to define the viability of using concrete of a certain composition in real applications. In this study, 15 Self-Compacting Concrete (SCC) mixtures produced with Recycled Concrete Aggregate (RCA) and Ground Granulated Blast Furnace Slag (GGBFS) were subjected to a monotonic-load test and a 5-cycle loading/unloading test with increasing maximum loads. Continuous monitoring of the applied loads and the SCC strain was performed. In the transversal direction, these tests caused the appearance of a yield step, cracking by vertical splitting, and higher levels of deformability than in the longitudinal direction. It was concluded that the RCA content of SCC should be defined according to serviceability conditions when used in compressed elements, to safeguard against failure due to transversal plastic strain.

1. Introduction

Concrete is not a continuous medium, due to the heterogeneity and lack of dislocations caused by its composition (cement, water, aggregate, and air) [1]. Its variable composition implies a mechanical performance in the hardened state of varying degrees of

* Corresponding author.
E-mail addresses: vrevilla@ubu.es (V. Revilla-Cuesta), mskaf@ubu.es (M. Skaf), amaia.santamaria@ehu.es (A. Santamaría), vortega@ubu.es (V. Ortega-López), jmmanso@ubu.es (J.M. Manso).
[1] Address: EPS. Calle Villadiego s/n. 09001 Burgos. Spain.
[2] Address: Escuela de Ingeniería de Bilbao, I (bloque B) - UPV/EHU. Plaza Ingeniero Torres Quevedo, 1. 48013 Bilbao. Spain.

https://doi.org/10.1016/j.conbuildmat.2021.123426
0950-0618/

complexity [2,3]. Furthermore, its workability is also of relevance in the fresh state and must be considered during the design process [4]. Self-Compacting Concrete (SCC) is one of the most outstanding concretes with regard to ease of placement, because it needs no vibration to fill formwork, due to its high flowability [5]. This type of concrete also shows a high mechanical strength when correctly designed [6]. The good strength behavior of SCC and the fact that no vibration is needed for its placement reduces energy consumption and significantly facilitates the filling of formwork [7,8], advantages that explain its ongoing study within the construction and building sector [9].

Concrete has a high stiffness that limits any internal strain, so its plastic behavior under compressive loading is not a widely studied field [10]. Likewise, internal strain causes cracking within concrete, which hinders the measurement of its strain when loading [11]. Nevertheless, the classical stress–strain curve of concrete is well-known: it initially shows an elastic linear section characterized by its modulus of elasticity [12] and, subsequently, a curved region of plastic deformation, with no clear separation between both zones [13]. Hence, a yielding region appears, in which the strain increases with a low variation in stress [14]. Although variations in concrete mix compositions will hardly modify the general pattern of behavior, they can cause specific modifications. For example, increasing the fines content will increase concrete workability [5] and the yield region of the curve [13]. Another example is the addition of fibers to concrete, which sew its cracks and increase the ultimate failure strain of the material [15,16]. On the other hand, the application of compressive stress causes tension within concrete in the transversal direction (circumferential or tangential), perpendicular to the direction of load application. The strain behavior of concrete in this direction in the elastic regime is defined by the Poisson's coefficient [8]. A value of 0.2 is assumed to be the conventional Poisson's coefficient to apply to concrete [3,17]. The authors of this research work have found no study that assesses the plastic behavior of non-confined concrete in the transversal direction.

The use of wastes as substitutes for cement clinker [18] and Natural Aggregate (NA) [19] to manufacture concrete is a major research line that aims to increase the sustainability of the construction sector [20]. Among the residues that have been validated as hydraulic binders [8], Ground Granulated Blast Furnace Slag (GGBFS) is one of the most outstanding [21]. Although previously used for soil stabilization [22], in recent years it has been used in the development of medium-strength concretes [23]. Steel slag [24] and construction and demolition waste [25] are examples of valid wastes for the optimal replacement of NA in different proportions [26], although in this study the behavior of Recycled Concrete Aggregate (RCA) is evaluated. This by-product, obtained by crushing rejected concrete precast components [27], has been used to develop concretes with good workability and strength [28]. In addition, it has even been used in recent years in non-conventional concretes, such as SCC [29].

Studies related to the addition of by-products to concrete, including SCC, have mainly been focused on their workability and mechanical properties [30] and on the behavior of structural elements [31]. However, the effect of these alternative materials on the plastic behavior of hardened concrete has not been studied in detail. It is known that the addition of GGBFS as a substitute for cement clinker decreases the modulus of elasticity of concrete [32]. Concerning RCA, only the influence of the coarse fraction on the stress–strain behavior of concrete in the longitudinal direction has been evaluated so far. Its usage reduces the strain levels upon fracture [33] and increases the cracking tendency of concrete [34]. Furthermore, it has been observed that pre-treatment of this waste can also alter the plastic behavior of concrete [35]: the use of coarse carbonated RCA decreases compressive strength, but increases strain at the maximum point of the stress–strain curve [36]. These aspects are specific alterations to plastic behavior, since the general shape of the stress–strain curve undergoes no significant change whenever the concrete composition is slightly modified [37].

In general, the stress–strain behavior of concrete under a plastic regime, in both the longitudinal and transversal directions, has hardly been studied. Furthermore, studies of concrete plastic behavior in the transversal direction have mainly been limited to concrete elements subjected to lateral confinement [38], regardless of whether NA or some type of waste was used in their manufacture [39,40]. The energy that can be released from concrete depends on these boundary conditions [41], which also limit its transversal deformability [42]. In that regard, this confinement improves the performance of recycled concrete more than the performance of concrete manufactured with NA [33,43]. The authors of this paper have found no other study that presents an analysis of transversal plastic behavior without confinement in any type of concrete. Hence, the objective of this study is to perform a detailed examination of the plastic performance of non-confined self-compacting concrete, which was chosen because it can be used in any structural application that demands high workability in the fresh state [6]. The additional inclusion of GGBFS and coarse and fine RCA enhances the global sustainability of these structural concretes. All these aspects are part of a broader research project conducted by the same research group, which addresses the behavior of SCC produced with these wastes/by-products.

A total of 15 self-compacting concrete mixes were produced with and without GGBFS and coarse RCA, and with different percentages and fractions of fine RCA. All mixtures were subjected to two tests for detailed evaluation of their strength and deformability [44]. On the one hand, a monotonic-load test was performed in which the load increased at a constant rate and, on the other hand, a low-cycle alternating load test, in which the specimens were subjected to successive loading/unloading cycles of increasing magnitude. In both tests, the load applied, and the longitudinal and transversal strain levels of the SCC were continuously monitored.

2. Materials and methods

In this section, an explanation is provided for each raw material in use, the composition of the different mixtures under study, and the experimental procedure developed for the analysis of the main aspects.

2.1. Materials

Two different types of cement were used according to EN 197–1 [45]: CEM I 52.5 R, with a density of 3.1 Mg/m^3 and a clinker content of 98%, and a sustainable CEM III/A 42.5 N, with a density of 3 Mg/m^3, and a content of around 45% GGBFS. Mains water was supplied from the urban water supply of Burgos, Spain, where the investigation took place. Two admixtures were used to achieve an optimum self-compactability of the mixtures: a viscosity regulator and a plasticizer, labelled A1 and A2 (admixtures 1 and 2), respectively.

In addition to GGBFS, some SCC samples incorporated RCA. This material was obtained by crushing rejected precast elements with a characteristic strength of 45 MPa. Its original granulometry, 0/31.5 mm, was separated into several fractions (4/12.5, 0/4, 1/4, 0/1, and 0/0.125 mm) by sieving, to obtain a maximum aggregate size suitable for SCC production (12.5 mm), and to study the effect of each RCA fraction in detail. When the coarse, fine and powder fractions of the mixtures were not 100% RCA, siliceous gravel

(4/12.5 mm) and/or sand (0/4 mm), limestone fines 0/1 mm and limestone filler (<0.063 mm) were added. The density and water absorption levels (EN 1097–6 [45]) of all the aggregates are shown in Table 1 and their gradation curves are depicted in Fig. 1.

2.2. Mixes design

Firstly, three self-compacting reference mixes labelled ICM, IIICM1 and IIICM2 were developed, in which the slump-flow design was between 700 and 850 mm (EN 12350–8 [45]). This flowability was achieved by adjusting the content of particles under 0.25 mm in accordance with the Fuller curve (see Fig. 2). These mixtures were produced with 100% NA in all fractions and with a range of cement types and amounts. Mix ICM was manufactured with CEM I, and mix IIICM1 with CEM III/A. In these two control mixes, the amount of cement was the same (300 kg/m^3). The cement content of mix IIICM2 was increased by 40% to provide a similar 28-day compressive strength to mixes ICM and IIICM2, as GGBFS provides lower strength than conventional cement clinker [46]. Furthermore, the admixtures proportion was in all cases the same: 2.3 kg/m^3 of A1 and 4.5 kg/m^3 of A2, respectively.

After developing the reference mixtures, twelve concrete mixes with RCA were designed, in which 100% coarse NA (size 4/12.5 mm) was replaced by RCA. Subsequently, different fine RCA contents and fractions (0/4, 1/4, 0/1, and 0/0.125 mm) were progressively added (in partial or total substitution of the fine NA and aggregate powder of the reference mixes), as explained below, due to the singularly high fine aggregate (size 0/4 mm) content of SCC, and due to its high sensitivity to changes in this aggregate fraction, particularly the aggregate powder [5]. Detailed in section 3.2, the mechanical tests of the mixtures yielded successful and coherent results that supported these progressive substitutions.

Finally, the "effective water-to-cement" ratio remained constant in all mixtures (0.50 in mixes with CEM I and 0.40 in mixes with CEM III/A), by increasing the water content to meet the water absorption (see Table 1) of the RCA after 15 min [30], which was the mixing time (see section 2.3).

The RCA mixes were labelled either *I* (CEM I) or *III* (CEM III/A) followed by the substitution percentage of NA 0/4 mm by RCA 0/4 mm. In addition, the letter *N* or *R* was added to some of the labels, depending on whether the aggregates smaller than 1 mm were either NA or RCA. The compositions of all the mixtures, once divided into the three batches detailed below, are shown in Table 2, Table 3 and Table 4, in which the different quantities are given in kg of each component per cubic meter of concrete.

- Batch 1. In this batch, the effects of both CEM I and CEM III/A, used in the same amounts, were assessed. The reference mix *par excellence* in this research work was ICM, although mixture ICM1 can also be considered a "partial reference" with regard to mixtures III50N, and III50R. First, the volume of the coarse fraction (4/12.5 mm) of NA was completely substituted by RCA 4/12.5 mm. Subsequently, 50% of fine NA 1/4 mm by volume was replaced with RCA of the same gradation (1/4 mm), in accordance with the results of a previous study of this research group [47], in which 50% fine NA was advanced as the maximum RCA replacement ratio for suitable mechanical behavior. The aggregate fraction 0/1 mm of these mixes was entirely NA. These two mixes were labelled I50N and III50N. Finally, as shown in Table 2, the aggregate fraction 0/1 mm of mixes I50N and III50N was replaced with RCA, thereby defining mixes I50R and III50R. This particular combination of RCA fractions maintained the self-compactability of concrete mixtures and, at the same time, meant that the effects of RCA 1/4 mm could be separately analyzed from the effects of RCA sized lower than 1 mm. This aspect was studied because RCA 0/1 and 0/0.125 mm are usually the RCA fractions that more than any others weaken concrete strength [48].
- Batch 2. In this batch, the reference mix, ICM, manufactured with type-I cement, and the full replacement of coarse NA with RCA were maintained. In addition, amounts of 0%, 50%, and 100% fine NA 0/4 mm were substituted by fine RCA 0/4 mm, resulting in mixes I0, I50, and I100. These replacement ratios of fine NA were also defined according to the performance observed in a previous study of this research group [47]. Additionally, the effect of adding RCA as aggregate powder was studied in mixture I100R, in which limestone fines 0/1 mm and limestone filler were replaced by RCA. The joint gradation of the batch 2 mixtures is shown in Fig. 2.
- Batch 3. This group includes all the mixes manufactured with CEM III/A, but with a higher content of cement, as previously explained. The reference mix was labelled IIICM2. Subsequently, mixes III0, III50, III100 and III100R were designed in the same way as the batch 2 mixes.

2.3. Mixing and testing

When an aggregate with high water absorption is used to produce concrete, staged mixing processes will maximize its water absorption and the workability of the concrete [49]. The mixing process that was performed therefore had three different stages: addition of the aggregate and half of the water; addition of the cement and the rest of water; and addition of the admixtures. After each stage, the concrete was mixed for 3 min and then left to rest for 2 min. These times were defined after different trials with mixing and resting times of between 1 and 5 min. Subsequently, the slump flow was checked (EN 12350–8 [45]) and six 10x20-cm cylindrical specimens were produced and placed in a moist room (humidity 95 ± 5% and temperature 20 ± 2 °C) until the performance of the following tests:

- Determination of compressive strength (EN 12390–3 [45]), modulus of elasticity, and the Poisson's coefficient (EN 12390–13 [45]) of all mixtures at 28 days on 2 specimens.
- Monotonic-load test, similar to standard compressive-strength tests, which consisted of the progressive displacement of the head frame at a constant rate.
- Loading/unloading test of increasing magnitude to evaluate the evolution of the stiffness of the mixtures. These last two tests were performed on two specimens after 90 days of curing, a point in time when many concrete structures are already in service [31].

In the second and third tests, the load applied and the effects of both longitudinal and transversal strain on the concrete were con-

Table 1
Physical properties of aggregates.

Aggregate	Saturated-surface-dry density (Mg/m^3)	15 min water absorption (%)	24 h water absorption (%)
RCA 4/12.5 mm	2.42	4.90	6.25
RCA 0/4 mm	2.37	5.77	7.36
RCA 1/4 mm	2.38	5.15	6.94
RCA 0/1 mm	2.36	6.26	7.47
RCA 0/0.125 mm	2.29	6.43	8.09
Siliceous gravel 4/12.5 mm	2.62	0.71	0.84
Siliceous sand 0/4 mm	2.58	0.18	0.25
Limestone fines 0/1 mm	2.62	0.38	0.53
Limestone filler < 0.063 mm	2.77	–	0.54

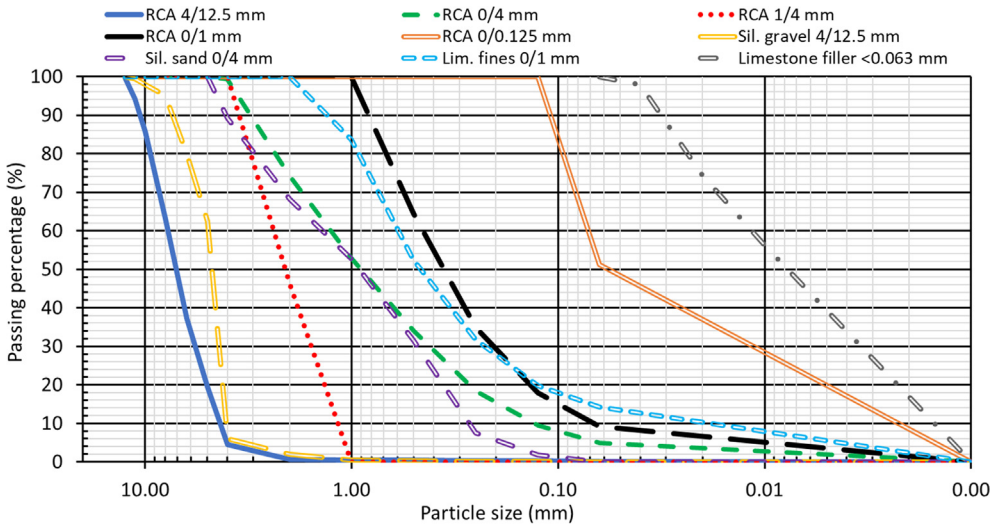

Fig. 1. Aggregate gradation.

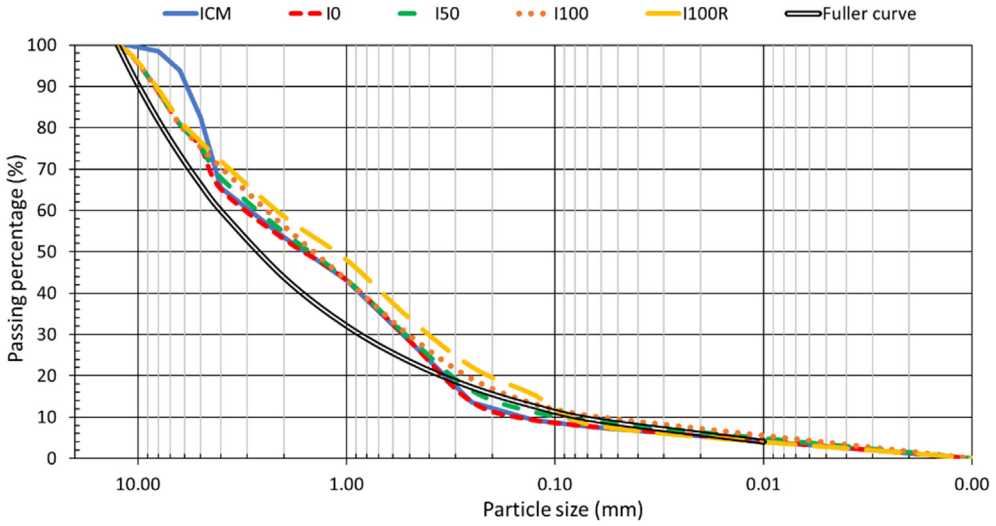

Fig. 2. Joint gradation of the batch 2 mixes.

Table 2
Composition of batch 1 mixes (kg per cubic meter).

	ICM	I50N	I50R[1]	IIICM1	III50N	III50R[1]
CEM I	300			0		
CEM III/A	0			300		
Water	170	200	225	170	200	225
Limestone fines 0/1 mm	225	430	0	225	430	0
Limestone filler < 0.063 mm	115		0	115		0
RCA 0/1 mm	0		385	0		385
RCA 0/0.125 mm	0		95	0		95
RCA 4/12.5 mm	0	530		0	530	
NA 4/12.5 mm	575	0		575	0	
RCA 1/4 mm	0	205		0	205	
NA 0/4 mm	940	475		940	475	

[1] Although these mixtures were labelled *R*, part of the aggregate fraction 0/1 mm was siliceous sand 0/4 mm.

tinuously recorded. The recording of the strain was done by six strain gauges, three in the longitudinal (vertical) direction and three in the transversal (circumferential or tangential) direction, evenly distributed around the perimeter of the specimen in the central zone of its shaft. 2 LVDTs set to measure loading piston displacement completed the measurements in the longitudinal direction. The applied load was measured with a calibrated load cell. A diagram of the test set up is shown in Fig. 3.

Table 3
Composition of batch 2 mixes (kg per cubic meter).

	ICM	I0	I50	I100	I100R
CEM I	300				
Water	170	185	210	235	255
Limestone fines 0/1 mm	225	0			
Limestone filler < 0.063 mm	115	0			
RCA 0/1 mm	0	200			
RCA 0/0.125 mm	0	95			
RCA 4/12.5 mm	0	530			
NA 4/12.5 mm	575	0			
RCA 0/4 mm	0	435	865		
NA 0/4 mm	940	475	0		

Table 4
Composition of batch 3 mixes (kg per cubic meter).

	IIICM2	**III0**	**III50**	**III100**	**III100R**
CEM III/A	**425**				
Water	**170**	**185**	**210**	**235**	**255**
Limestone fines 0/1 mm	**225**	**0**			
Limestone filler < 0.063 mm	**115**	**0**			
RCA 0/1 mm	**0**	**200**			
RCA 0/0.125 mm	**0**	**95**			
RCA 4/12.5 mm	**0**	**430**			
NA 4/12.5 mm	**440**	**0**			
RCA 0/4 mm	**0**	**435**	**865**		
NA 0/4 mm	**940**	**475**	**0**		

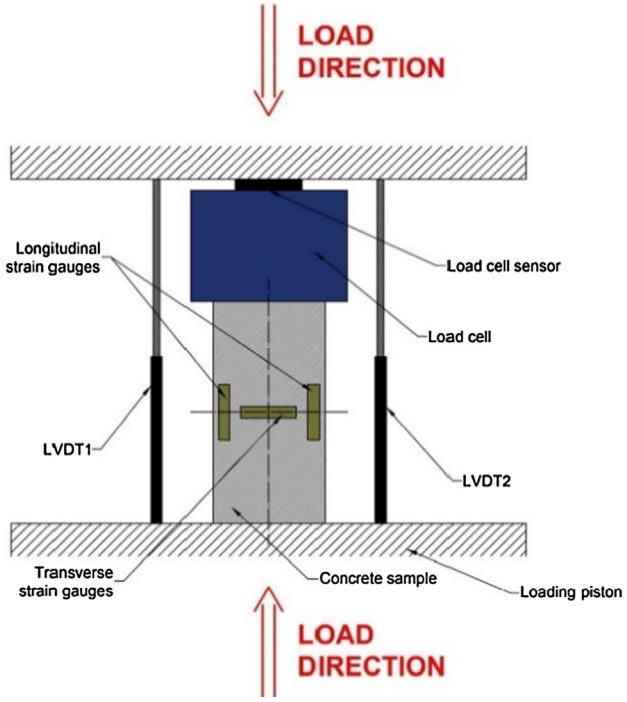

Fig. 3. Assembly diagram for data recording.

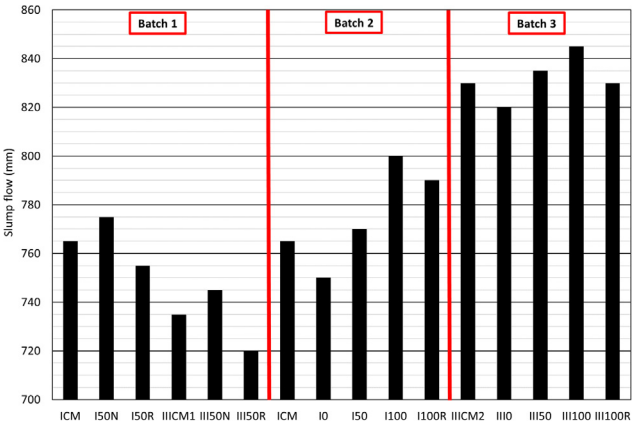

Fig. 4. Slump flow of the mixes.

3. Results and discussion

In this section, the results of the different tests indicated in the experimental plan are reported.

3.1. Fresh behavior: slump-flow test

All the mixtures had the defined target slump flow at the beginning of the study, between 700 and 850 mm, as shown in Fig. 4. All changes made to the composition of the mixtures modified the slump flow:

- CEM III/A has a higher grinding fineness than CEM I, which hinders the uniform dragging of aggregate particles in SCC [32]. Therefore, when the quantity of both cements remained constant, the use of CEM III/A reduced the slump flow (batch 1 mixtures). However, the decrease of the coarse aggregate content improved the slump flow of the CEM III/A mixtures in comparison with the CEM I mixtures (batches 2 and 3) [50].
- The irregular shape of coarse RCA compared to siliceous gravel [13] decreased the slump flow of the mixtures when it was incorporated.
- Finally, the higher content of particles smaller than 0.25 mm of RCA 0/4 mm compared to siliceous sand (see Fig. 1) yielded a more compact cement paste that dragged the aggregate particles more easily [5]. Therefore, the higher the content of RCA 0/4 mm, the higher the slump flow, although it was reduced with the use of RCA as aggregate powder (mixes I50R, III50R, I100R, and III100R), possibly due to its more irregular shape compared to limestone fines 0/1 mm and filler.

3.2. Compressive strength and elastic properties

Compressive strength, modulus of elasticity and the Poisson's coefficient values at 28 and 90 days of all the mixtures of the three batches are shown in Fig. 5. The compressive strengths and the moduli of elasticity, as well as their temporal increase (from 28 to 90 days) [47], decreased with the addition of all RCA fractions in all the batches [2]. Regarding the absolute values of both properties, the inclusion of coarse RCA rather than coarse NA signified a notable loss of concrete strength (I0 and III0 versus ICM, and IIICM2, respectively), due to weaker Interfacial Transition Zones (ITZ) [2]. The partial substitution of fine NA by fine RCA caused even greater loss of strength (50 N and I50 versus ICM; III50N versus IIICM1; and III50 versus IIICM2), due to the presence of mortar particles in this RCA fraction, as well as increased adherence problems between the aggregate and the cementitious matrix [47]. The total replacement of NA with RCA increased this damage even more (I100 and III100 versus I50 and III50, respectively). Finally, the effects of RCA aggregate powder additions (I50R versus I50N; III50R versus III50N; I100R versus I100; and III100R versus III100) could be qualified as dramatic, as the compressive strength of mixes I50R, III50R, I100R and III100R never even reached the minimal value for structural concrete (20 MPa) [3,17]. The smaller the RCA fraction that was used, the more damaging its effect on the mechanical behavior of concrete [51]. The use of CEM III/A in higher amounts (batch 3 mixes) hardly modified the effect of RCA, although it yielded higher compressive strengths than those of batch 2 mixes, despite the similar compressive strengths of the reference mixes (ICM and IIICM2). The higher cement content could have partially compensated the negative effects of the RCA [52].

The temporal increase was greater when CEM III/A was used, because of its slower development of strength [46]. However, as has been stated, the growing presence of RCA reduced this temporal increase. Thus, the compressive-strength increase in both absolute and percentage terms was 3.3 (5.8%) and 5.6 (9.4%) MPa for reference mixes ICM and IIICM2, respectively; 1.3 (2.9%) and 2.5 (5.1%) MPa for mixes I0 and III0; and only 0.7 (2.8%) and 1.7 (4.9%) MPa for mixtures I100R and III100R.

The addition of any RCA fraction decreased the Poisson's coefficient at 28 days, while the use of CEM III/A increased it. Furthermore, this coefficient generally decreased over time, especially when using CEM I (a decrease from 28 to 90 days of 5.1 and 4.3% for mixes I50N and I0 respectively, and only 3.9 and 1.4% for mixes III50N and III0) and RCA 0/4 mm (decrease from 28 to 90 days of 9.9 and 6.9% for mixes I100 and III100). However, the addition of the finest RCA fractions (0/1 and 0/0.125 mm) increased the value of this coefficient over time, possibly due to the increase of transversal deformability that resulted from the delayed release of water absorbed by these RCA fractions during mixing [49].

3.3. Monotonic-load test

The monotonic-load test and the compressive-strength test were performed in similar ways, although the applied load and both longitudinal and transversal concrete strain levels were continuously recorded during the former test. Previous trials demonstrated that undesired sudden failure of the specimens, which might hinder strain measurements [37], was avoided by setting the load application rate at 1 kN/s. This rate was lower than the standard recommendation in ASTM C39 [53], 2.2 kN/s, but no problem was detected during the performance of the test. Data were recorded at a frequency of 20 Hz.

3.3.1. Longitudinal direction

The stress–strain curves using conventional engineering variables for compressive tests underlined the aspects indicated in the introduction, as shown in Fig. 6 (right-hand-side curves): a linear elastic section followed by a plastic curved zone with no clear separation between both [3,17]. A quasi-linear elastic region probably existed after the proportionality limit before the plain yielding region was reached. The main values of this curve for all the mixtures are shown in Table 5: the modulus of elasticity, the limit of proportionality, the point of maximum stress (thereafter peak point) and the strain at final fracture.

The addition of 100% coarse RCA not only decreased the strength and the modulus of elasticity of the mixtures, as explained in section 3.2 [48], but also the strain at peak point and fracture point by around 12% (mixture I0 versus ICM, and mixture III0 versus IICM2), as has also been shown in other studies [33].

The addition of fine RCA decreased the stiffness and strength of SCC and increased its plastic deformability [54]. On the one hand, the higher the amounts of RCA fractions, the greater the deformability of the mix at peak point and at fracture point. On the other, the replacement of CEM I by CEM III/A caused a similar effect to fine RCA, although the increase in the total binder content (batch 3 mixtures) decreased that deformability.

The expressions and values in current concrete standards approximate the main results of the stress–strain curve. These expressions and values provide safe estimates for conventional concretes.

- The peak strain can be calculated by eq. (1) of the model code of the International Federation for Structural Concrete (CEB-FIP) [55], in which $f_{c,m}$ and ε_0 are, respectively, the stress (MPa) and the peak strain (‰) measurements. Both in EC2 [3] and in ACI 318–19 [17], this value is estimated at 2,000 με.

$$\varepsilon_0 = 0.7\hat{A} \cdot {f_{c,m}}^{0.31} \quad (1)$$

- Strain at fracture is estimated at 3,000 με, according to ACI 318–19 [17], and at 3,500 με, according to EC2 [3].

The theoretical values of both peak strain and strain at fracture of ACI 318–19 were lower than the experimental values, thus providing a reliable estimate. However, mixtures I50R, IIICM1, III50R, I100, I100R, and III100R (6 of the 15 mixes, all with by-products) reached a higher strain than 3,500 με at fracture, a value defined by EC2. Finally, the trend shown by eq. (2) of the CEB-FIP for peak strain was only fulfilled in mixes with 100% fine NA (ICM, I0, IIICM1, IIICM2, and III0), as the loss of compressive strength, due to the addition of fine RCA, increased rather than reduced the peak strain. Table 6 depicts a comparison of these deformation values.

3.3.2. Transversal direction

The curves of longitudinal stress versus transversal strain are shown in Fig. 6 (left-hand-side curves), and their most representative values appear in Table 7. These curves initially presented a linear elastic zone with a high slope with no observable microstructural damage to the material. The Poisson's coefficient was around 0.2 units, the precise values of which are shown in Table 7 (columns of elastic behavior). This linear elastic region ended at a variable transversal strain of 150–185 με (except mix III50R, Table 7) and a stress value practically equal to the proportional limit in the longitudinal direction that is specified in Table 5; hence, both measurements showed an equally coherent proportional limit. The geometric evolution could be qualified as "barreling", due to the barrel shape of a centered bulge and a constraint in both bases, as shown in Fig. 7a.

Subsequently, a short region with a decreasing slope (between the proportional limit and the start point of yield step, see Fig. 6) occurred, showing a stress increase of 3–4 MPa and a strain

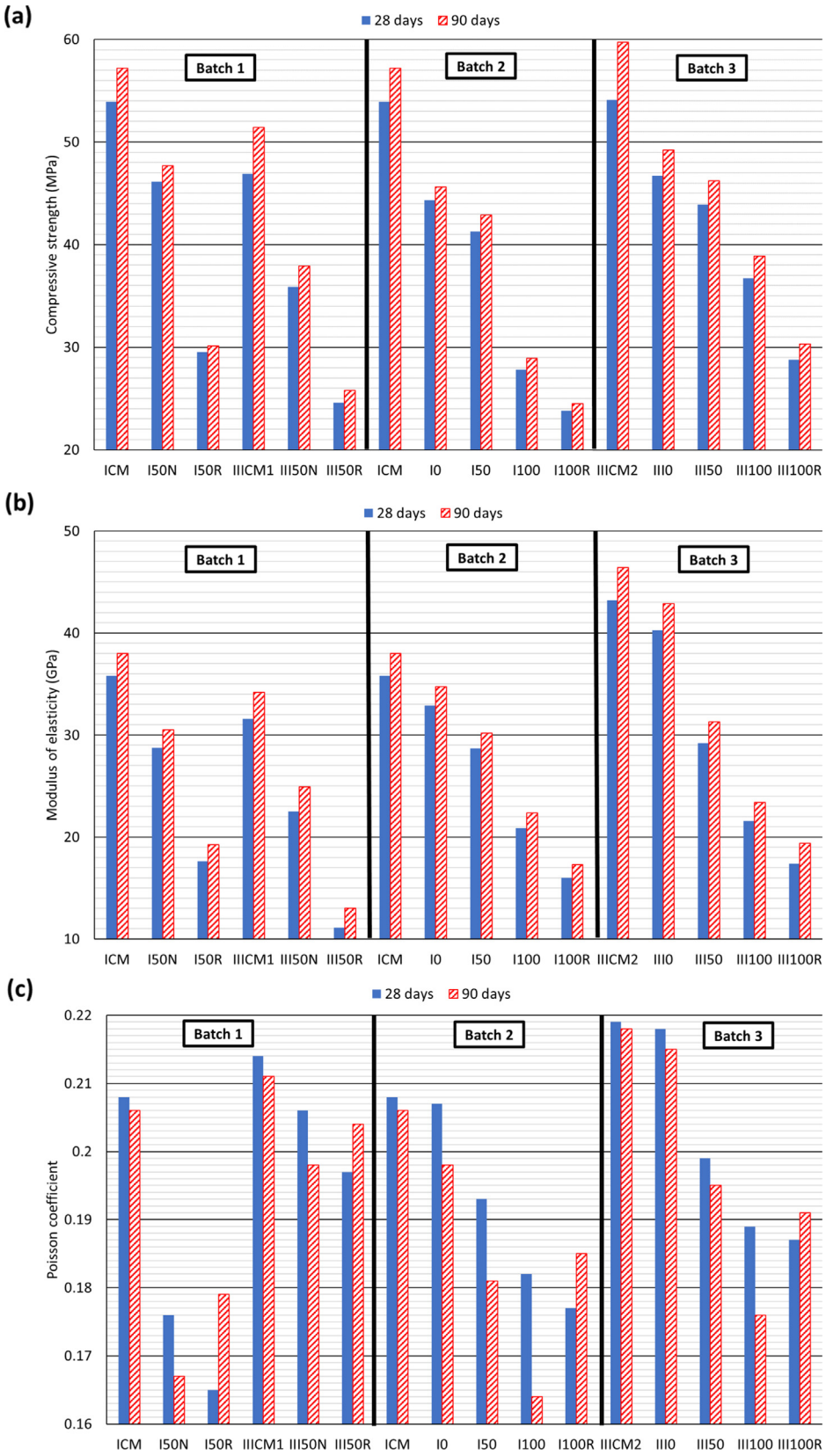

Fig. 5. Temporal evolution of (a) compressive strength; (b) modulus of elasticity; (c) Poisson's coefficient.

increase of 30–50 με. This region approximately represents the "start of global yielding", focused on the start of micro-structural damage (micro-cracking) in the perimeter region of the zone with the highest bulge (center of the specimen, Fig. 7b), in which the tensile transversal strain began to exceed the threshold strain that the material can withstand.

That region was followed by a quasi-linear region with a very low (almost horizontal) slope; similar to a yield step in a tensile

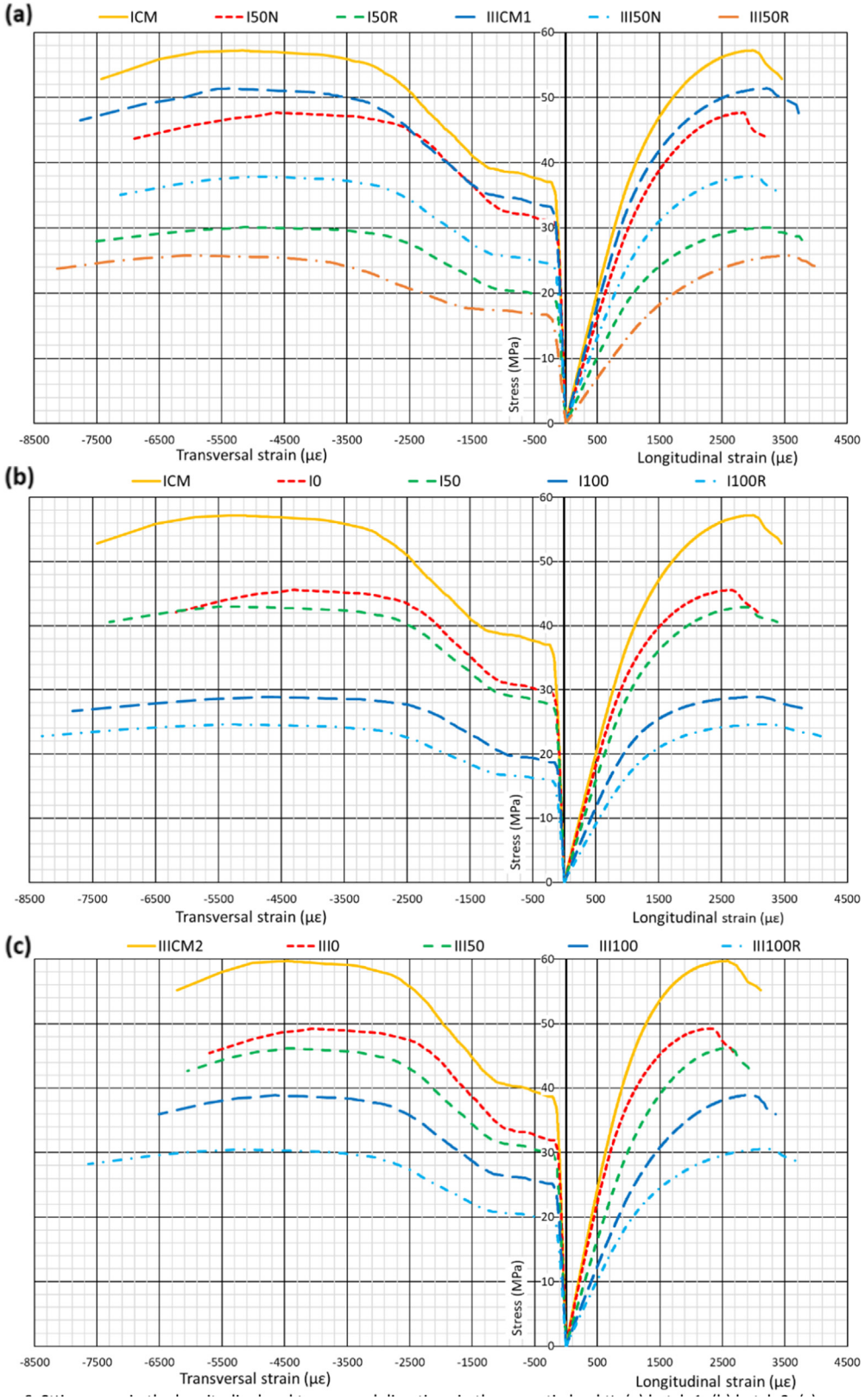

Fig. 6. Stress–strain curves in the longitudinal and transversal directions in the monotonic-load test: (a) batch 1; (b) batch 2; (c) batch 3.

test of structural steel. This yield region was extended until the "final point of yield step", shown under the columns of plastic behavior in Table 7. A plastic-strain zone with slight micro-structural damage, in which the transversal strain of the concrete increased from 150 to 185 to around 1,000 με and the stress increased in the order of 1–2 MPa. This increase in transversal tensile strain was associated with generalized micro-cracking of the specimen increasing the micro-structural damage, moving from the situation in Fig. 7b to the situation in Fig. 7c. The micro-cracking was produced by vertical splitting, *i.e.*, the cracks were generated on the

Table 5
Main values of stress–strain curves in the longitudinal direction. For the proportional limit and the strain at fracture, the ratio (%) to the peak point appears between brackets.

		ELASTIC BEHAVIOR			PLASTIC BEHAVIOR		
		Modulus of elasticity (GPa)	Proportional limit		Peak point		Strain at fracture (με)
			Stress (MPa)	Strain (με)	Stress/compressive strength (MPa)	Strain (με)	
Batch 1	ICM	39.6	33.2 (58.0)	873 (29.1)	57.2	2,996	3,452 (115.2)
	I50N	31.8	27.9 (58.5)	915 (32.1)	47.7	2,847	3,228 (113.4)
	I50R	20.1	16.8 (55.8)	875 (26.7)	30.1	3,277	3,808 (116.2)
	IIICM1	35.6	30.0 (58.4)	877 (27.2)	51.4	3,220	3,754 (116.6)
	III50N	26.0	22.6 (59.6)	908 (30.2)	37.9	3,003	3,454 (115.0)
	III50R	13.6	15.3 (59.3)	1,177 (32.4)	25.8	3,632	4,125 (113.6)
Batch 2	ICM	39.6	33.2 (58.0)	873 (29.1)	57.2	2,996	3,452 (115.2)
	I0	36.2	25.9 (56.8)	746 (28.1)	45.6	2,659	3,073 (115.6)
	I50	31.5	25.7 (59.9)	851 (29.1)	42.9	2,923	3,386 (115.8)
	I100	23.3	17.4 (60.2)	777 (24.9)	28.9	3,115	3,925 (126.0)
	I100R	18.0	13.8 (56.1)	798 (24.4)	24.6	3,272	4,071 (124.4)
Batch 3	IIICM2	48.4	35.8 (60.0)	771 (29.8)	59.7	2,589	3,111 (120.2)
	III0	44.7	28.3 (57.5)	660 (28.4)	49.2	2,324	2,685 (115.5)
	III50	32.6	27.5 (59.5)	879 (33.6)	46.2	2,616	2,952 (112.8)
	III100	24.4	22.5 (57.8)	962 (32.4)	38.9	2,967	3,352 (113.0)
	III100R	20.2	18.4 (60.3)	948 (29.2)	30.5	3,247	3,762 (115.9)

Table 6
Comparison between experimental and theoretical values in the longitudinal direction.

		MODULUS OF ELASTICITY (GPa), ASTM C469M-14	STRAIN AT PEAK POINT (με)			FINAL STRAIN AT FRACTURE (με)		
			Theoretical value		Experimental value	Theoretical value		Experimental value
			CEB-FIP [55]	ACI 318–19 [17], EC2 [3]		EC2 [3]	ACI 318–19 [17]	
Batch 1	ICM	39.6	2,454	2,000	2,996	3,500	3,000	3,452
	I50N	31.8	2,320		2,847			3,228
	I50R	20.1	2,011		3,277			3,808
	IIICM1	35.6	2,374		3,220			3,754
	III50N	26.0	2,160		3,003			3,454
	III50R	13.6	1,917		3,632			4,125
Batch 2	ICM	39.6	2,454		2,996			3,452
	I0	36.2	2,288		2,659			3,073
	I50	31.5	2,245		2,923			3,386
	I100	23.3	1,986		3,115			3,925
	I100R	18.0	1,889		3,272			4,071
Batch 3	IIICM2	48.4	2,487		2,589			3,111
	III0	44.7	2,342		2,324			2,685
	III50	32.6	2,297		2,616			2,952
	III100	24.4	2,178		2,967			3,352
	III100R	20.2	2,019		3,247			3,762

lateral periphery of the test specimen, a zone under greater strain and stress due to the bulging of the specimen. They then propagated in both vertical directions throughout the specimen and progressively penetrated towards its central vertical axis on vertical planes, as shown in Fig. 7b and Fig. 7c. In addition, this micro-cracking was slow and progressive, so it produced no sudden release of mechanical energy. The generalization of micro-cracking caused a notable increase in the transversal strain of the sample specimen and, at the same time, a significant increase in its apparent (contouring) volume associated with the bulge-barreling.

From the final point of the yield step to the maximum-stress point (peak point), these curves continued showing a plastic behavior, associated with growth of the damaged region, from the situation of Fig. 7c to the situation shown in Fig. 7d. The slope of the curves was firstly higher, but it progressively decreased until the peak point. The zone of the slope reduction (around 3,000 με) in this plastic region probably corresponded to the situation shown in Fig. 7d. The low slopes of this region of the curve, to the left and to the right of the peak point, were associated with a hardly foreseeable behavior in the damaged regions. At the maximum point of this curve (peak point), transversal strain levels of between 4,500 and 6,000 με were recorded, corresponding to increased stress levels of around 31%. Finally, 14 of the 15 mixtures showed a fracture strain of over 6,000 με. Specimen micro-cracking was widespread at the final moment of fracture under compression.

The high transversal strain of the concrete, due to its micro-cracking, produced a high increase in the apparent-contour volume of the specimens. This increase was associated with a value of the "apparent Poisson's coefficient" of around a theoretical limit of 0.5 units in the plastic zone. A situation that undoubtedly establishes a clear limit for the practical use of this concrete in engineering elements, in terms of mechanical stress: the starting point of the yield step, which corresponded to the Poisson's coefficients of approximately 0.2 units (62–65% strain at fracture, proportional limit, see Table 7), must never be exceeded in service loads.

On the basis of the aspects addressed in both this section and the previous one, it can initially be concluded that the concrete samples showed a linear-elastic behavior under compression and tension. They lost the linearity under compression when cracking appeared along vertical-radial planes (due to tensile tangential-circumferential stresses that appear in horizontal planes), became generalized, and changed both the conditions of the geometric regularity of the tested samples (barreling due to the friction con-

Table 7
Characteristic values of stress–strain behavior in the transversal direction. The values between brackets are the percentage ratios (%) in relation to the peak point.

		ELASTIC BEHAVIOR					PLASTIC BEHAVIOR				
		Poisson's coefficient	Proportional limit		Start point of yield step		Final point of yield step		Peak point		Strain at fracture (με)
			Stress (MPa)	Strain (με)	Stress (MPa)	Strain (με)	Stress (MPa)	Strain (με)	Compressive strength (MPa)	Strain (με)	
Batch 1	ICM	0.206	33.2 (58.0)	180 (3.5)	37.1 (64.9)	204 (3.9)	39.3 (68.7)	1,211 (23.4)	57.2	5,165	7,427 (143.8)
	I50N	0.167	27.8 (58.3)	152 (3.3)	30.3 (63.5)	192 (4.2)	32.7 (68.6)	1,025 (22.2)	47.7	4,612	6,906 (149.7)
	I50R	0.179	17.0 (56.5)	158 (3.1)	19.6 (65.1)	195 (3.9)	20.6 (68.4)	1,117 (22.1)	30.1	5,062	7,613 (150.4)
	IIICM1	0.211	29.9 (58.2)	184 (3.4)	33.8 (65.8)	213 (4.0)	35.8 (69.6)	1,382 (25.8)	51.4	5,361	7,763 (144.8)
	III50N	0.198	22.5 (59.4)	179 (3.6)	24.4 (64.4)	201 (4.1)	26.0 (68.6)	1,179 (23.8)	37.9	4,960	7,124 (143.6)
	III50R	0.204	15.4 (59.7)	202 (3.4)	16.5 (64.0)	234 (3.9)	17.7 (68.6)	1,560 (25.9)	25.8	6,027	8,147 (135.2)
Batch 2	ICM	0.206	33.2 (58.0)	180 (3.5)	37.1 (64.9)	204 (3.9)	39.3 (68.7)	1,211 (23.4)	57.2	5,165	7,427 (143.8)
	I0	0.197	25.8 (56.6)	146 (3.4)	29.7 (65.1)	181 (4.2)	31.2 (68.4)	1,016 (23.7)	45.6	4,288	6,172 (143.9)
	I50	0.181	25.8 (60.1)	155 (3.3)	27.9 (65.0)	212 (4.4)	29.4 (68.5)	1,036 (21.7)	42.9	4,768	7,233 (151.7)
	I100	0.164	17.3 (59.9)	127 (2.7)	18.1 (62.6)	164 (3.4)	19.8 (68.5)	886 (18.6)	28.9	4,762	7,820 (164.2)
	I100R	0.185	13.6 (55.3)	145 (2.7)	15.9 (64.6)	193 (3.7)	16.9 (68.7)	1,078 (20.4)	24.6	5,286	8,302 (157.1)
Batch 3	IIICM2	0.218	35.9 (60.1)	169 (3.8)	38.9 (65.1)	199 (4.5)	40.7 (68.2)	1,123 (25.2)	59.7	4,451	6,222 (139.8)
	III0	0.215	28.5 (57.9)	143 (3.6)	31.8 (64.6)	211 (5.3)	33.7 (68.5)	973 (24.2)	49.2	4,016	5,697 (141.9)
	III50	0.195	27.6 (59.7)	172 (3.9)	29.8 (64.5)	215 (4.9)	31.7 (68.6)	1,124 (25.4)	46.2	4,419	6,052 (137.0)
	III100	0.176	22.3 (57.3)	168 (3.6)	25.3 (65.0)	228 (4.9)	26.7 (68.6)	1,149 (24.7)	38.9	4,650	6,505 (139.9)
	III100R	0.191	18.6 (61.0)	183 (3.5)	19.5 (63.9)	237 (4.6)	20.9 (68.5)	1,197 (23.0)	30.5	5,206	7,638 (146.7)

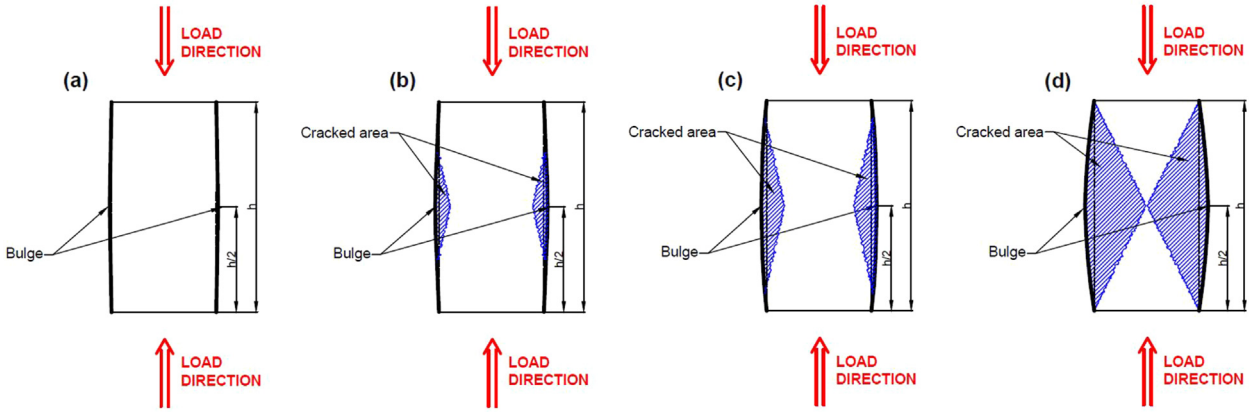

Fig. 7. Bulging and cracking of a concrete cylindrical sample under compressive loading: (a) elastic region without irreversible damage; (b) halfway intermediate point with partial damage; (c) halfway intermediate point with more extended damage; (d) generalized damage at peak point.

straint in both bases) and the internal homogeneity of the material, which became heterogeneous. At this point, instability due to (meso- or micro-) bulging and buckling occurred at many points within the cracked region, and the apparent global behavior of the tested sample was not linear, but plastic or yielding. Hence this vertical cracking, at the beginning superficial and subsequently deeper, involved decisive damage to the material and caused high strains recorded in the transversal direction.

Concerning the influence of the concrete components on mechanical behavior, it can be stated that in the transversal direction, the use of 100% coarse RCA increased the elastic and plastic stiffness of the concrete specimens, as shown by the decrease in both the Poisson's coefficient and the strain at fracture (see Table 7). The effect of the fine fraction of this residue was the same for the elastic zone, but different in the plastic zone, because when this RCA fraction was incorporated in the SCC, its plastic deformability increased. The joint use in the mixtures of both RCA fractions, 100% coarse RCA and 50% fine RCA, produced strain levels and a plastic behavior that were similar in the mixtures with 100% NA. Mixtures with CEM III/A in the same amount as CEM I also increased their deformability. In this way, mix III50R had a strain at fracture of 8,147 με. On the other hand, the increase of binder content (batch 3 mixes) increased the plastic stiffness of the mixes, despite the higher deformability of the GGBFS compared to the conventional cement clinker. Thus, mix III0 showed a strain at fracture of only 5,697 με, 43% less than mix III50R (8,147 με). Regardless of the composition of the mixture, the ratio between the stress and strain at the most representative points of the curve and the values at the maximum point of the curve were similar in all the mixtures (see Table 7).

3.3.3. Relationship between transversal and longitudinal strain levels

The monotonic-load test results showed a close relationship between the strain of the concrete in both the longitudinal and transversal directions, as may be seen in Fig. 8, which represents this magnitude versus the percentage of applied stress with respect to the compressive strength of each mixture. This relationship was similar in all the mixtures, regardless of their composition. Initially, it had a constant value, equal to the Poisson's coefficient, up to approximately 60–65% of the compressive strength. Then, the relationship was an almost vertical line, due to the large increase in transversal strain within the yielding zone. The transversal strain equaled the longitudinal strain when 67–70% of the compressive strength was reached. Subsequently,

another approximately constant region was obtained with a quotient value of 1.3–1.6 up to 95% of the compressive strength. At this point, the ratio suddenly increased until reaching the maximum point of the stress–strain curve, in which the transversal strain was 1.6–1.8 times the longitudinal strain. Finally, the transversal strain reached twice the longitudinal strain at the fracture point.

3.3.4. Volumetric variation

The variation of the external volume of the specimens (enveloping volume) throughout the monotonic-load test is depicted in Fig. 9, in which this magnitude and the applied stress are shown by the rectilineal coordinates of the graph. The plastic regions of the corresponding curves of the different mixes are clearly similar to those of Fig. 6 that represent transversal strain versus stress (left-hand-side curves). The difference was evident (negative volumetric variation) in the elastic region, due to the contraction of the specimens with no notable bulging.

Several hypotheses and simplifications that also refer to other calculations are needed to obtain these curves of relative volumetric variation regarding the geometric form of the bulging (or barreling) of the specimens depicted in Fig. 7:

- The form of the vertical profile of the specimens (transversal section, Fig. 7) was chosen as parabolic (eq. (2)), in which "*2b*" is the total height of the specimen, and "*a*" is the increase of the diameter of the specimens in half of their height. The integrated area of this parabola above the y-axis is given by 4ab/3, and the position of the mass center is roughly approximated by 3a/8.

$$y = a\hat{\mathrm{A}}\cdot\left(1-\frac{x^2}{b^2}\right) \tag{2}$$

- The application of Pappus-Guldin's second theorem yielded eq. (3), which provided the bulging volume of the specimen (ΔV). In this formula, D is the diameter of the specimen. In this way, the total volume V_t of the specimen is approximated by eq. (4).

$$\Delta V = \pi\hat{\mathrm{A}}\cdot a\hat{\mathrm{A}}\cdot b\hat{\mathrm{A}}\cdot\left(a+\frac{4\hat{\mathrm{A}}\cdot D}{3}\right) \tag{3}$$

$$V_t = \frac{\pi\hat{\mathrm{A}}\cdot D^2\hat{\mathrm{A}}\cdot b}{2}+\Delta V \tag{4}$$

- If ΔV is divided by V_t, the transversal volumetric variation, due to the dilatation (bulging) in this direction, is calculated with eq. (5) (ε_t is the transversal strain). In this calculation, the very small magnitudes, such as *a,* can be disregarded whenever in summation with very much larger magnitudes, such as *D.*

$$\frac{\Delta V}{V_t}=\frac{8\hat{\mathrm{A}}\cdot a}{3\hat{\mathrm{A}}\cdot D}=\frac{8}{3}\hat{\mathrm{A}}\cdot\varepsilon_t \tag{5}$$

- Finally, it is necessary to substract the volumetric contraction in the longitudinal direction, *i.e.*, the longitudinal strain, ε_l. The volumetric variation ($\Delta V/V_O$) of the specimens is provided by eq. (6).

$$\frac{\Delta V}{V_O}=\frac{8}{3}\hat{\mathrm{A}}\cdot\varepsilon_t-\varepsilon_l \tag{6}$$

In verification of these calculations, we must locate a volumetric contraction in the elastic field given by one of the Hooke-Poisson's formulas (eq. (7), where σ_h is the hydrostatic stress and K is the volumetric coefficient according to eq. (8), which depends of the modulus of elasticity and the Poisson's coefficient). Considering ordinary values that are suitable for the mixes such as a Poisson's coefficient of 0.2, a modulus of elasticity of 35 GPa and $\sigma_h = \sigma_z/3$, where the vertical stress, σ_z, is around 35 MPa in the elastic region, a negative value (contraction) of the volumetric variation ($\Delta V/V_O$) of 0.6‰ is obtained, as depicted in Fig. 9.

$$\frac{\Delta V}{V_O}=-\frac{\sigma_h}{K} \tag{7}$$

$$K=\frac{E}{3\hat{\mathrm{A}}\cdot(1-2\hat{\mathrm{A}}\cdot\upsilon)} \tag{8}$$

3.4. Loading/unloading test

If a material is loaded until it moves into a plastic regime and is then unloaded, the unloading will theoretically occur linearly. The slope of this line is the modulus of elasticity (Fig. 10a) and when the unloading finishes the material will present residual strain, as depicted in the graph. If the material is loaded again, the new loading line will coincide with the previous unloading one [56]. However, the material actually presents hysteresis and, generally, a slight increase of its stiffness during the unloading is observed, as well as a slight decrease in its elastic stiffness in the subsequent loading process (Fig. 10b) [33].

The mixtures developed in this study were subjected to a loading/unloading test of 5 cycles, to evaluate the above-mentioned behavior. In each cycle, the maximum applied stress was progressively increased, as shown in Table 8. In the first two cycles, 25% and then 40% of the compressive strength obtained in the monotonic-load test were applied, in order to evaluate the variations of their theoretical elastic behavior. In the third cycle, the maximum load applied was slightly lower (around 1–2 MPa) than the proportional limit; hence the tests applied around 55% of compressive strength. The aim of this third cycle was to study the performance of the mixtures after applying the maximum usual stress considered in the design of concrete structures (see discussion in section 3.3.2).

The fourth cycle evaluated the behavior of the mixtures when they underwent significant plastic strain. Therefore, the maximum load of this cycle was around 80% of the maximum value reached in the monotonic-load test. Finally, the specimens were broken in the fifth and last cycle, and the variations of the peak stress, the peak strain, and the strain at fracture (Table 9 and Table 10) were analyzed. In these loading/unloading tests, the load application rate was also 1 kN/s, and a minimum load of 1 kN was maintained throughout the whole test to avoid any slippage of the specimens. Data collection was performed at 20 Hz.

3.4.1. Longitudinal direction

As shown in Fig. 11, the stress–strain behavior in the longitudinal direction of the mixtures in this cyclic test progressively deviated from the theoretical behavior indicated in Fig. 10a. The application of a load equal to 25% of the compressive strength (first cycle), notably below the proportional limit, caused a mismatch with the previously explained theoretical behavior that was practically negligible. In the second cycle (40% of the compressive strength), a little hysteresis and residual strain (from 40 to 60 με, see Table 9) appeared, with no significant change of stiffness during the loading test. Furthermore, the unloading section of the curves (see Fig. 11) was slightly curved in this cycle, which meant

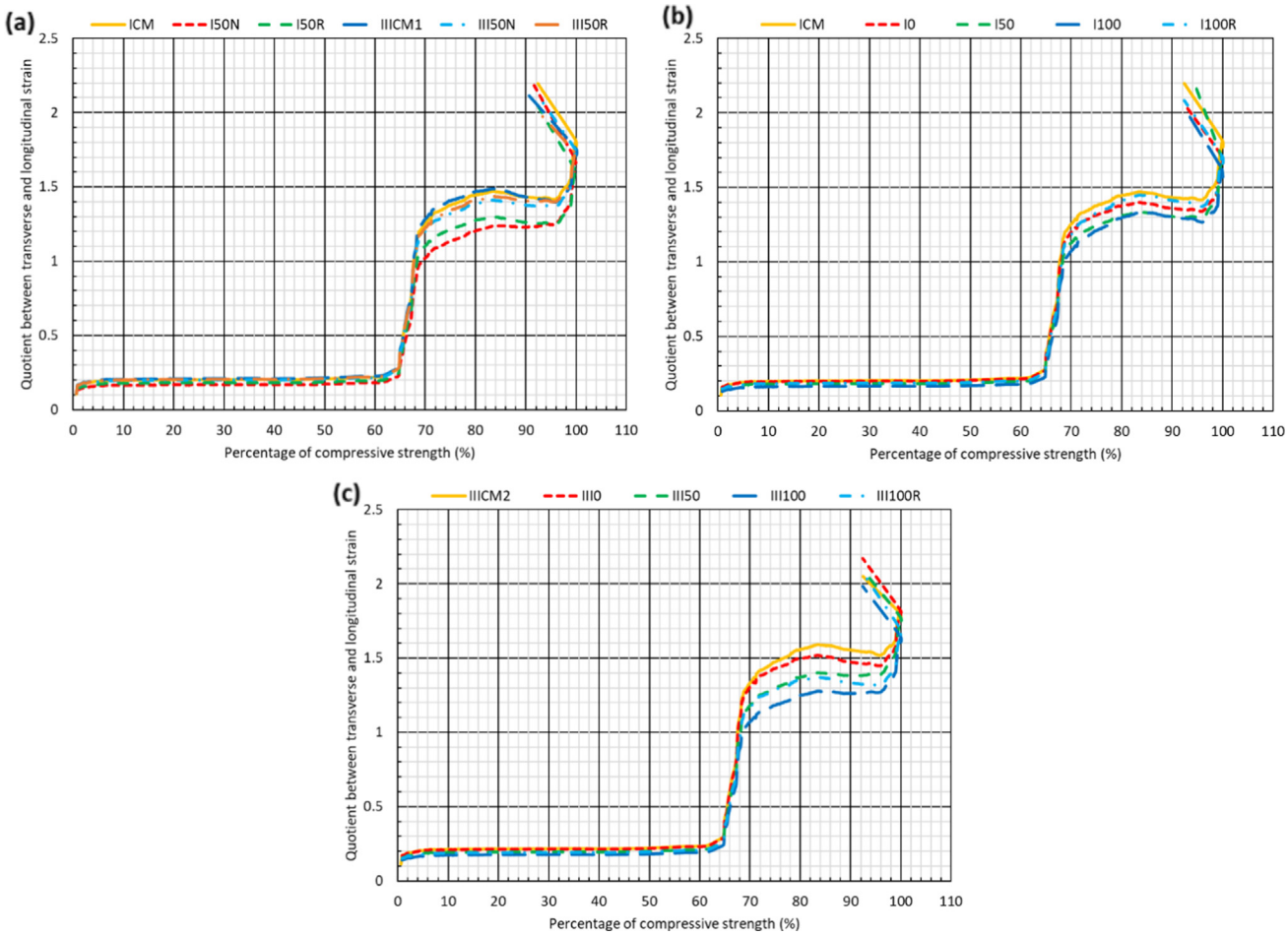

Fig. 8. Relationship between transversal and longitudinal strain in the monotonic-load test: (a) batch 1; (b) batch 2; (c) batch 3.

that it was not coincident with the loading of the third cycle. Although theoretically, the applied load in this second cycle was lower than the stress corresponding to the proportional limit (see Table 8), local creep behavior was observed at a crystalline scale in the Calcium-Silicate-Hydrate (C-S-H) gel, reminiscent of the beginning of a plain creep test [8]. In practical terms, due to its lengthy duration, this kind of test is a realistic superposition between an elastic–plastic loading regime and creep-yielding, which is representative of engineering concrete structures in which the in-service load is submitted to variations of high intensity-severity (for instance, flyovers and railway bridges).

The incipient behavior observed in the second cycle increased in subsequent cycles, in which notably enhanced hysteretic regions appeared. The modulus of elasticity decreased throughout these cycles, while the remaining strain increased. In addition, micro-structural damage may be suspected at around the start of the third cycle, due to the change in behavior experienced by the mixtures, although it is difficult to verify its importance in current terms. This issue is explained in detail in section 3.4.2.

The loading regions of the graphics from these last cycles were curved, so the elastic modulus was calculated by considering the points of the loading section corresponding to 5 and 25% of the compressive strength obtained in the monotonic-load test (see Table 9). The failure stress (Table 8) and the strain at fracture (Table 9) were lower than those obtained in the monotonic-load test.

The loss of strength and strain at fracture ranged between 4 and 14 % for all mixtures. Regardless of the amount of cement added to the mix, the loss of strength was greater when using CEM III/A, although the use of this type of cement reduced the decrease in strain at fracture. In terms of deformability, the mixes with GGBFS therefore withstood the application of increasing cyclic load better than conventional cement clinker, although their strength behavior was worse. As with the monotonic-load test, the addition of 100% coarse RCA increased the brittleness of the mixtures and increased the percentage loss of strength and deformability. On the contrary, the higher deformability of fine RCA compensated for this decrease: compressive strength and strain at fracture decreases were 10.3 and 6.1% for mixture ICM, 13.8 and 12.4% for mixture I0, and 3.3 and 9.0% for mixture I100R. The residual strain after each cycle was in percentage terms similar in all the mixtures, regardless of their composition.

The addition of 100% coarse RCA had no appreciable effect on the evolution of the modulus of elasticity throughout the test, as shown by the results of mixtures ICM and I0, and IIICM2 and III0. However, the effect of fine RCA 0/4 mm depended on the amount of cement added to the mix. In the CEM I mixtures, the loss of the modulus of elasticity increased with additions of RCA. On the contrary, in the batch 3 mixtures (produced with CEM III/A and 40% more cement than the batch 2 mixtures), the higher the amount of fine RCA, the lower the decrease in the modulus of elasticity. Moreover, mixture I100 showed the maximum decrease in the modulus of elasticity (38.4%). The delayed release of water absorbed by RCA 0/1 mm and 0/0.125 mm during mixing [49] meant that the effect of these fractions was exactly the opposite: reduced loss of stiffness of the CEM I mixtures and increased stiffness of the CEM III/A mixtures. Finally, mixtures with up to 50% RCA 0/4 mm showed a higher modulus of elasticity in the second cycle than in the first one, which meant that the addition of large

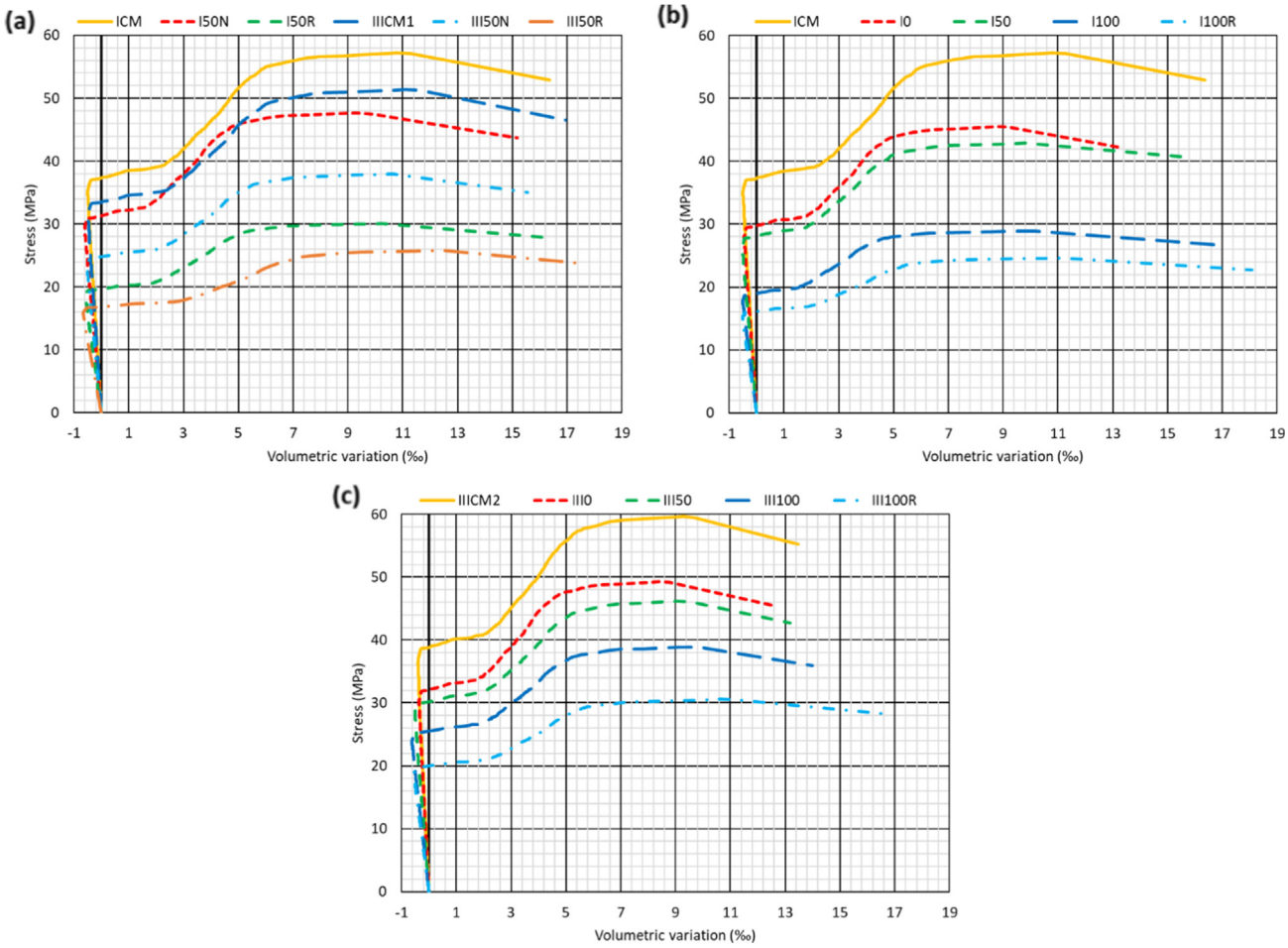

Fig. 9. Relationship between volumetric variation versus stress in the monotonic-load test: (a) batch 1; (b) batch 2; (c) batch 3.

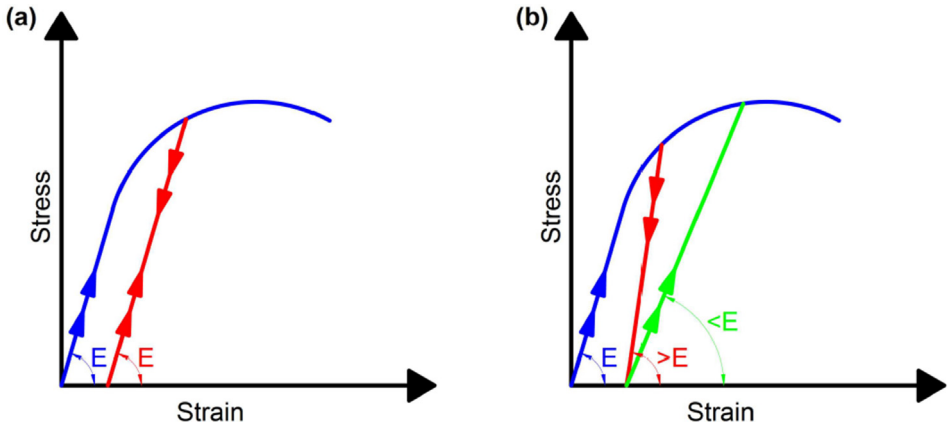

Fig. 10. Loading/unloading process: (a) theoretical situation; (b) real situation.

amounts of fine RCA reduced the ability of the mixtures to maintain their initial stiffness following compressive stress.

3.4.2. Transversal direction

The longitudinal stress versus transversal strain curves throughout the five test cycles (Fig. 12 and Table 10) showed similarities with those obtained in the longitudinal direction: non-coincidence of load/unload regions, decreased stress and strain at fracture with respect to the values of the monotonic-load test, and increased deformability with the number of cycles. All the mixtures showed a highly defined linear elastic behavior during the first two cycles, under loading lower than 40% of their compressive strength.

In the third cycle, the theoretically applied stress never exceeded the proportional limit of the mixtures estimated in the monotonic-load test (see Fig. 12), so it could be hypothetically assumed that the transversal strain should not be associated with obvious damage, which could otherwise be confirmed by the lack

Table 8
Maximum stress (MPa) applied in each cycle of the loading/unloading test. For the 5th cycle, the percentage decrease of the failure stress in relation to the compressive strength is displayed in brackets.

		1st cycle	2nd cycle	3rd cycle	4th cycle	5th cycle	PL	CS
Batch 1	ICM	15.6	24.0	32.1	45.8	51.3 (-10.3)	33.2	57.2
	I50N	12.7	19.5	26.2	38.2	41.8 (-12.4)	27.9	47.7
	I50R	8.3	12.8	16.2	24.1	27.4 (-9.0)	16.8	30.1
	IIICM1	13.7	21.1	28.3	41.1	45.3 (-12.1)	30.0	51.4
	III50N	10.0	15.3	20.6	30.2	32.8 (-13.5)	22.6	37.9
	III50R	6.8	10.4	14.0	20.6	22.3 (-13.6)	15.3	25.8
Batch 2	ICM	15.6	24.0	32.1	45.8	51.3 (-10.3)	33.2	57.2
	I0	11.9	18.4	24.6	36.5	39.3 (-13.8)	25.9	45.6
	I50	11.5	17.8	23.8	34.3	38.0 (-11.4)	25.7	42.9
	I100	8.1	12.4	16.7	23.1	26.6 (-8.0)	17.4	28.9
	I100R	7.2	11.1	12.9	19.7	23.8 (-3.3)	13.8	24.6
Batch 3	IIICM2	16.0	24.6	33.0	47.8	52.7 (-11.7)	35.8	59.7
	III0	12.4	19.1	27.1	39.3	40.8 (-17.1)	28.3	49.2
	III50	12.0	18.4	26.2	36.9	39.4 (-14.7)	27.5	46.2
	III100	10.8	16.7	21.4	31.2	35.7 (-8.2)	22.5	38.9
	III100R	8.8	13.6	18.2	24.9	29.1 (-4.6)	18.4	30.5

PL: stress (MPa) at the proportional limit according to the monotonic-load test.
CS: compressive strength (MPa) according to the monotonic-load test

Table 9
Most representative values of the longitudinal stress–strain behavior in the loading/unloading test.

		1st cycle		2nd cycle		3rd cycle		4th cycle		5th cycle	
		E (GPa)	S (με)	E (GPa)	S (με)	E (GPa)	S (με)	E (GPa)	S (με)	E (GPa)	FS (με)
Batch 1	ICM	38.1	14 (0.4)	38.8 (+1.8)	47 (1.5)	35.0 (-8.1)	118 (3.6)	29.8 (-21.8)	381 (11.8)	28.6 (-24.9)	3,241 (-6.1)
	I50N	30.3	14 (0.5)	30.5 (+0.7)	49 (1.7)	28.5 (-5.9)	118 (4.1)	26.4 (-12.9)	349 (12.3)	26.1 (-13.9)	2,894 (-10.3)
	I50R	19.3	14 (0.4)	19.4 (+0.5)	50 (1.4)	17.0 (-11.9)	130 (3.8)	14.4 (-25.4)	419 (12.0)	14.3 (-25.9)	3,458 (-9.2)
	IIICM1	34.2	13 (0.4)	34.6 (+1.2)	46 (1.3)	28.6 (-16.4)	128 (3.7)	25.1 (-26.6)	398 (11.5)	23.6 (-31.0)	3,461 (-7.8)
	III50N	24.9	13 (0.4)	25.1 (+0.8)	46 (1.5)	22.2 (-10.8)	119 (3.8)	15.6 (-37.3)	370 (11.9)	18.9 (-24.1)	3,125 (-9.5)
	III50R	12.9	17 (0.4)	13.0 (+0.8)	61 (1.6)	12.0 (-7.0)	150 (3.9)	10.8 (-16.2)	454 (11.7)	10.5 (-18.6)	3,849 (-6.7)
Batch 2	ICM	38.1	14 (0.4)	38.8 (+1.8)	47 (1.5)	35.0 (-8.1)	118 (3.6)	29.8 (-21.8)	381 (11.8)	28.6 (-24.9)	3,241 (-6.1)
	I0	34.3	12 (0.4)	34.7 (+1.2)	40 (1.5)	30.8 (-10.2)	103 (3.8)	27.3 (-20.4)	318 (11.9)	26.4 (–23.0)	2,691 (-12.4)
	I50	30.3	13 (0.4)	30.5 (+0.7)	44 (1.4)	24.7 (-18.5)	124 (3.8)	21.8 (-28.1)	384 (11.5)	21.2 (-30.0)	3,241 (-4.3)
	I100	22.4	12 (0.3)	21.6 (-3.6)	44 (1.3)	17.3 (–22.8)	124 (3.6)	14.6 (-34.8)	402 (11.6)	13.8 (-38.4)	3,472 (-11.5)
	I100R	17.2	14 (0.4)	16.5 (-4.1)	51 (1.4)	14.1 (-18.0)	136 (3.7)	12.5 (-27.3)	419 (11.3)	11.6 (–32.6)	3,704 (-9.0)
Batch 3	IIICM2	46.3	12 (0.4)	46.8 (+1.1)	40 (1.4)	41.3 (-10.8)	103 (3.6)	36.2 (-21.8)	321 (11.6)	34.2 (-26.1)	2,778 (-10.7)
	III0	42.8	10 (0.4)	43.1 (+0.7)	34 (1.5)	38.7 (-9.6)	85 (3.7)	33.9 (-20.8)	266 (11.5)	31.8 (-25.7)	2,315 (-13.8)
	III50	31.4	13 (0.5)	31.6 (+0.6)	44 (1.7)	29.9 (-4.8)	106 (4.2)	28.0 (-10.8)	311 (12.4)	27.9 (-11.1)	2,547 (-13.7)
	III100	23.4	15 (0.5)	23.0 (-1.7)	55 (1.8)	22.8 (-2.6)	126 (4.1)	21.5 (-8.1)	367 (12.1)	21.0 (-10.3)	3,067 (-8.5)
	III100R	19.4	15 (0.4)	19.0 (-2.1)	55 (1.6)	17.4 (-10.3)	135 (3.9)	15.7 (-19.1)	409 (11.8)	15.1 (–22.2)	3,473 (-7.7)

E: modulus of elasticity (GPa); S: remaining strain at the end of the cycle (με); FS: strain at fracture point (με).
Values in brackets are:
For the modulus of elasticity, the percentage variation of its value regarding the value in the first cycle.
For the remaining strain, the percentage that it represents with respect to the strain at fracture after the fifth cycle.
For the strain at fracture, the decrease from the values of this strain obtained in the monotonic-load test.

of residual strain, perhaps for the same reasons as proposed in section 3.3.2. However, that hypothetical assumption is false, because micro-structural damage in this third cycle occurred in most of the mixtures, with the exception of mixes ICM, IIICM1, and IIICM2 (reference mixtures with 100% coarse and fine NA). As much is substantiated in Fig. 12 where two types of behavior were obtained during the loading period of the fourth cycle, which are key to any analysis of these test results. In general, the graph of the mixtures was similar to the curve obtained for mix I50N or I50R (Fig. 12a), in which the slope of the fourth cycle load region was notably lower than the loading regions in the previous cycles. However, the aforementioned exceptions, mixes ICM, IIICM1, and IIICM2, presented a curve with two loading regions for the fourth cycle (Fig. 12). The first region clearly coincided with the loading–unloading of the third cycle, and the second region of loading underwent a remarkable loss of slope, flattening out until the point of maximum loading in the cycle. The other mixtures (100% coarse RCA) showed a remarkably smaller load slope at the beginning of the fourth cycle than the load slope of the third cycle, which constitutes evidence of generalized and irreversible damage at the micro-structural level generated throughout the third cycle.

Among all the mixtures, the "plastic behavior" in the fourth cycle showed some similarity with the behavior of the concrete material described in section 3.3.2, as local micro-cracking had damaged it, as shown in Fig. 7. This zone was associated with a loss of slope in the loading region of the curves shown in Fig. 12, starting from a certain level of loading, clearly shown at the point of inflection leading to the flattening out of the curves of mixtures ICM, IIICM1, and IIICM2, though less well defined in the other mixes, that might be roughly situated within the interval of 45–55% of the compressive strength of the mixture. Residual strain between 800 and 2,000 με after the unloading of this fourth cycle confirmed this performance.

Therefore, the addition of 100% coarse RCA had significant effects on the behavior of the mixtures in this fourth cycle:

- The mixtures manufactured with 100% NA in the coarse and fine fractions withstood the damage caused by the variable loading better than all others, as they retained their stiffness in the elas-

Table 10
Most representative values of the transversal stress–strain behavior in the loading/unloading test.

		1st cycle		2nd cycle		3rd cycle		4th cycle		5th cycle	
		ν	S (με)	ν	S (με)	ν	S (με)	N	S (με)	ν	FS (με)
Batch 1	ICM	0.205	2 (0)	0.209 (2.0)	9 (0.1)	0.189 (-9.8)	25 (0.4)	0.156 (-25.9)	1,032 (15.3)	2.096 (920.5)	6,750 (9.1)
	I50N	0.166	1 (0)	0.167 (0.6)	10 (0.2)	0.157 (-5.4)	22 (0.4)	0.698 (320.5)	1,191 (20.8)	2.198 (1,224.1)	5,737 (16.9)
	I50R	0.179	1 (0)	0.181 (1.1)	13 (0.2)	0.150 (-16.2)	23 (0.3)	0.622 (247.5)	1,274 (18.9)	2.082 (1,063.1)	6,730 (11.6)
	IIICM1	0.211	1 (0)	0.214 (1.4)	12 (0.2)	0.176 (-16.6)	24 (0.3)	0.160 (-24.2)	1,097 (15.4)	2.148 (918.0)	7,176 (7.6)
	III50N	0.198	3 (0)	0.199 (0.5)	11 (0.2)	0.176 (-11.1)	25 (0.4)	0.750 (278.8)	1,358 (20.6)	2.340 (1,081.8)	6,597 (7.4)
	III50R	0.204	2 (0)	0.206 (1.0)	15 (0.2)	0.189 (-7.4)	34 (0.5)	0.671 (228.9)	1,489 (20.0)	2.148 (952.9)	7,458 (8.5)
Batch 2	ICM	0.205	2 (0)	0.209 (2.0)	9 (0.1)	0.189 (-9.8)	25 (0.4)	0.156 (-25.9)	1,032 (15.3)	2.096 (920.5)	6,750 (9.1)
	I0	0.198	1 (0)	0.201 (1.5)	8 (0.2)	0.178 (-10.1)	22 (0.4)	0.713 (260.1)	1,107 (21.0)	2.174 (998.0)	5,278 (14.5)
	I50	0.181	3 (0)	0.182 (0.6)	11 (0.2)	0.148 (-18.2)	22 (0.3)	0.685 (278.5)	1,286 (19.8)	2.218 (1,125.4)	6,482 (10.4)
	I100	0.164	2 (0)	0.158 (-3.7)	12 (0.2)	0.127 (–22.6)	19 (0.3)	0.728 (343.9)	1,429 (20.3)	2.253 (1,273.8)	7,056 (9.8)
	I100R	0.185	1 (0)	0.177 (-4.3)	15 (0.2)	0.151 (-18.4)	25 (0.4)	0.756 (308.6)	1,548 (20.3)	2.284 (1,134.6)	7,630 (8.1)
Batch 3	IIICM2	0.217	1 (0)	0.220 (1.4)	7 (0.1)	0.194 (-12.0)	21 (0.4)	0.167 (-24.4)	878 (15.3)	2.140 (884.8)	5,741 (7.7)
	III0	0.215	3 (0)	0.216 (0.5)	6 (0.1)	0.194 (-9.8)	20 (0.4)	0.799 (271.6)	1,036 (21.2)	2.335 (986.0)	4,876 (14.4)
	III50	0.195	2 (0)	0.196 (0.5)	8 (0.2)	0.185 (-5.1)	24 (0.5)	0.760 (289.7)	1,155 (21.9)	2.298 (1,078.5)	5,278 (12.8)
	III100	0.176	1 (0)	0.173 (-1.7)	12 (0.2)	0.171 (-2.8)	26 (0.4)	0.731 (315.3)	1,309 (21.7)	2.177 (1,136.9)	6,023 (7.4)
	III100R	0.191	3 (0)	0.186 (-2.6)	13 (0.2)	0.171 (-10.5)	28 (0.4)	0.747 (291.1)	1,492 (20.6)	2.308 (1,108.4)	7,228 (5.4)

ν: Poisson's coefficient; S: residual strain at the end of the cycle (με); FS: strain at fracture (με); CS: compressive strength (MPa).
Values between brackets represent:
For the Poisson's coefficient, the percentage variation in its value relative to the value in the first cycle.
For the residual strain, the percentage that it represents with respect to the strain at fracture of the fifth cycle.
For strain at fracture, the decreasing values compared to the ones obtained in the monotonic-load test.

tic zone. In addition, the load under which the plastic behavior began in the fourth cycle was approximately 2 MPa greater than the maximum load in the third cycle.
- The mixes manufactured with 100% coarse RCA, regardless of the fine RCA content or the type of cement used, largely decreased in elastic stiffness from the third cycle. This performance can be attributed to the fact that the damage affected the ITZ between the coarse RCA and the cementitious matrix more significantly than when NA was used.

The behavior in the fifth cycle was the same in all the mixtures, with a large increase in the elastic compliance (loading) compared to that obtained in the initial cycles, and notable hysteresis with respect the unloading of the fourth cycle. As with the monotonic-load test, the post-failure yielding section showed a more ductile fracture than the one produced in the longitudinal direction.

3.4.3. Relationship between transversal and longitudinal strain

The relationships between the transversal and the longitudinal strains are depicted in Table 10 (Poisson's coefficient from elastic region) and in Fig. 13. It must be recalled that the Poisson's coefficient displayed in Table 10 was calculated using the strain gauge data in the interval of loading from 5 to 25% of compressive strength. During the first three cycles, this relationship was approximately constant, and its value approximately coincided with the Poisson's coefficient displayed in Table 10. This coefficient showed a slight decrease from the first to the third cycle associated with the slight hysteresis in each cyclic load. The values of this coefficient in the fourth and fifth cycle are improper, due to the absence of pure elastic behavior and could be qualified as "fictitious Poisson's coefficients".

Once again, the most notable difference occurred in the fourth cycle between mixtures that either incorporated 100% coarse RCA or otherwise, as was described in the previous section. In Table 10, the values of the Poisson's coefficient for the mixtures ICM, IIICM1, and IIICM2 in the fourth cycle were even slightly lower than in the earlier cycles. However, considering the fourth cycle globally (see Fig. 13), it can be seen that the differences between the mixtures tended to mitigate over this cycle. The values of this "fictitious Poisson's coefficient" were between 1.2 and 1.7 units at maximum load, and between 2.6 and 3.9 units after unloading; this behavior was associated with greater barreling of the specimens.

Finally, the loading of the fifth cycle roughly coincided with the unloading of the fourth cycle in all the mixtures. The relationship between both strains at the peak point (ultimate stress) was 1.7–2.3 units. This value was roughly coincident with the values corresponding to the ultimate stresses of the mixtures observed in Fig. 8.

4. Conclusions and recommendations

In this paper, the elastic and plastic stress–strain behavior in both the longitudinal and the transversal directions of a Self-Compacting Concrete (SCC) containing Recycled Concrete Aggregate (RCA) and Ground Granulated Blast Furnace Slag (GGBFS) in varying proportions has been compared with a conventional SCC containing natural aggregates (NA) as a reference mixture. The 15 mixtures manufactured with and without GGBFS and coarse RCA, and different contents and fractions of fine RCA were tested up to failure in conventional compressive tests, under monotonic compressive loading and under cyclic loading/unloading processes, in which the maximum applied load increased over the cycles. The following conclusions can be drawn from the aspects discussed throughout this article:

- In all cases, the additions of both coarse and fine RCA decreased the compressive strength, modulus of elasticity, and Poisson's coefficient of the concrete, *i.e.*, the mechanical behavior of the RCA concrete was notably worse than that of NA concrete. The addition of RCA should therefore be carefully studied when using this waste to produce structural concretes with high-load bearing capacity.
- The stress–strain behavior of the mixtures both in the longitudinal and in the transversal directions under monotonic compressive loading showed important differences. First, a yield step was only noted in the transversal direction. Second, the plastic yielding deformability was much higher in the transversal direction, so that the strain at fracture in that direction was approximately twice as high as in the longitudinal direction. These two phenomena were associated with the appearance of vertical cracking in the contour of the test specimen.

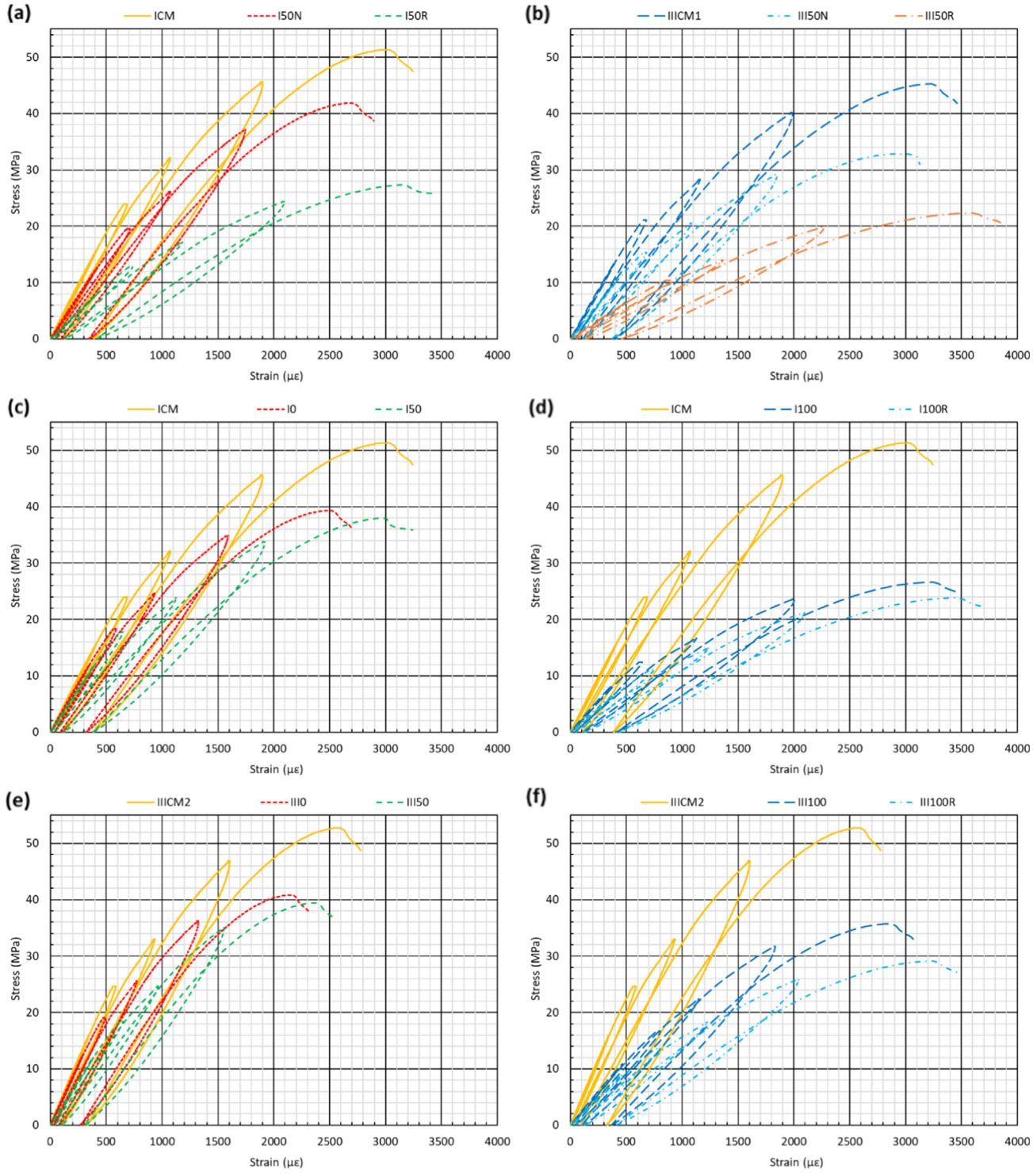

Fig. 11. Longitudinal stress–strain behavior in the loading/unloading test: (a, b) batch 1; (c, d) batch 2; (e, f) batch 3.

- The use of coarse RCA decreased strain at fracture, while the addition of fine RCA increased it. These additions meant that mixtures with 100% NA and mixtures with 100% and 50% coarse and fine RCA, respectively, had almost identical strain levels at fracture. The total replacement of the traditional cement clinker by CEM III/A in the same amounts also increased the plastic deformability of the mixtures and, consequently, both the longitudinal and the transversal strain at fracture.
- The application of loading/unloading cycles of growing severity increased deformability throughout the cycles and reduced the compressive strength of the mixtures and their strain at fracture. The stress–strain behavior in the longitudinal direction was not dependent on the composition of the mixture. Nevertheless, mixture composition was a key performance factor in the transversal direction, because the mixtures with coarse RCA experienced a higher increase in their elastic deformability

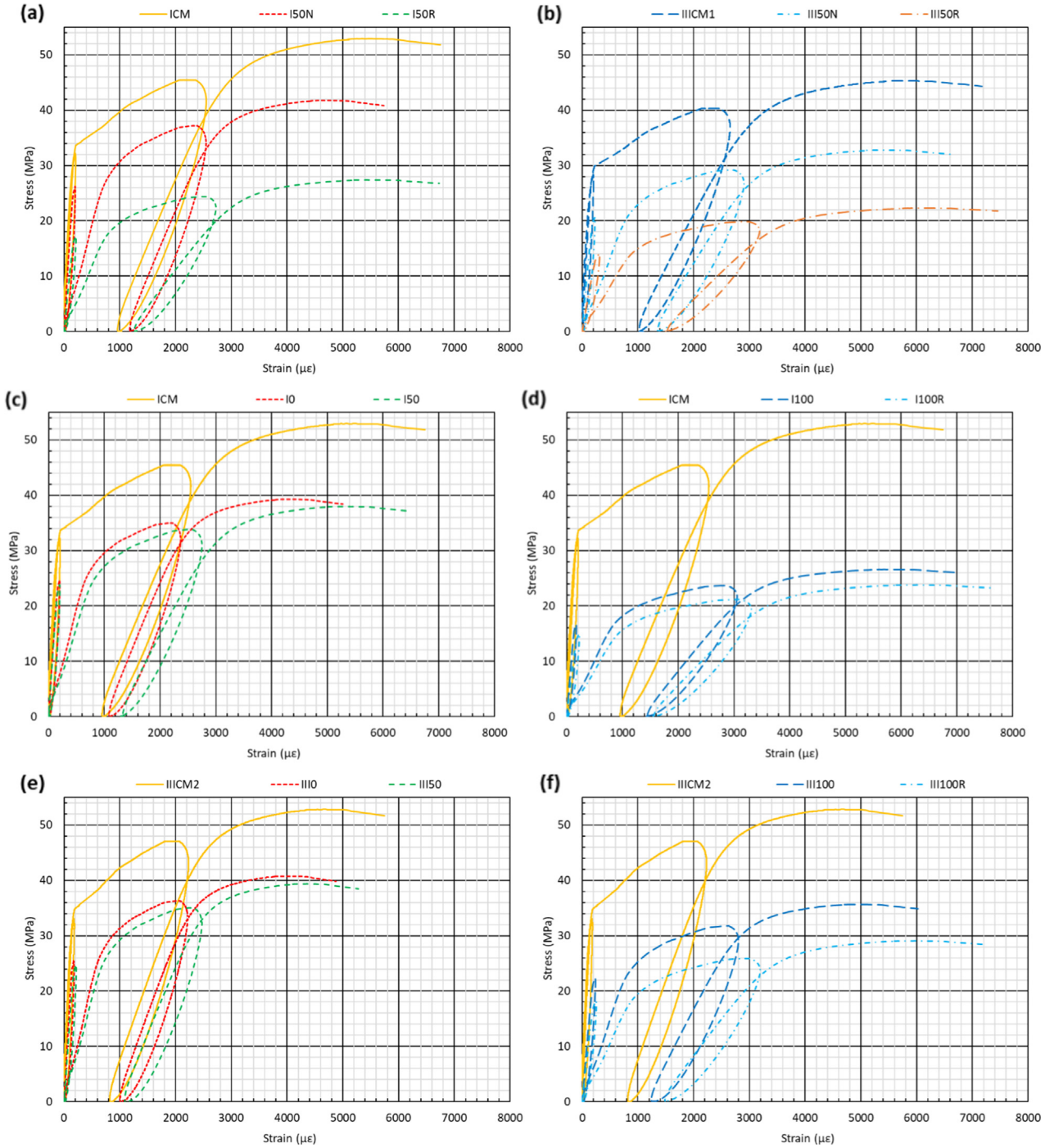

Fig. 12. Transversal stress–strain behavior in loading/unloading test: (a, b) batch 1; (c, d) batch 2; (e, f) batch 3.

when they were subjected to a small plastic strain (55% failure stress), tripling the Poisson's coefficient. In mixtures with 100% NA, this behavior occurred when 75–80% of the failure stress was applied. However, the yield step disappeared, due to micro-cracking during the cycles applied before reaching this zone of the curve. The effects of RCA and the cement type were very similar in the monotonic-load test.

A comparison of the results of both tests shows that the damage accumulated in the first three cycles in the loading/unloading test reduced the "admissible" stress from 62 to 65 % of the failure load in NA mixtures to<55% in mixtures containing RCA. From an engineering point of view, the generalized damage mentioned in section 3.4.2 is an undesirable situation that should be avoided in structural concrete elements designed to support variable mechanical stresses. Therefore, RCA should be used with caution, and the amount of RCA added to the SCC mixes should be defined and limited according to serviceability conditions rather than conventional failure design. In this way, no tensile damage will be observed due to transversal strain when the concrete is subjected to axial loading, and SCC with RCA can be successfully used.

Finally, from all the above, it is clear that the addition of RCA and GGBFS significantly modified not only the elasticity of the mixes, but also their plastic, stress–strain behavior in both directions. This area of research, with very few studies, is therefore of

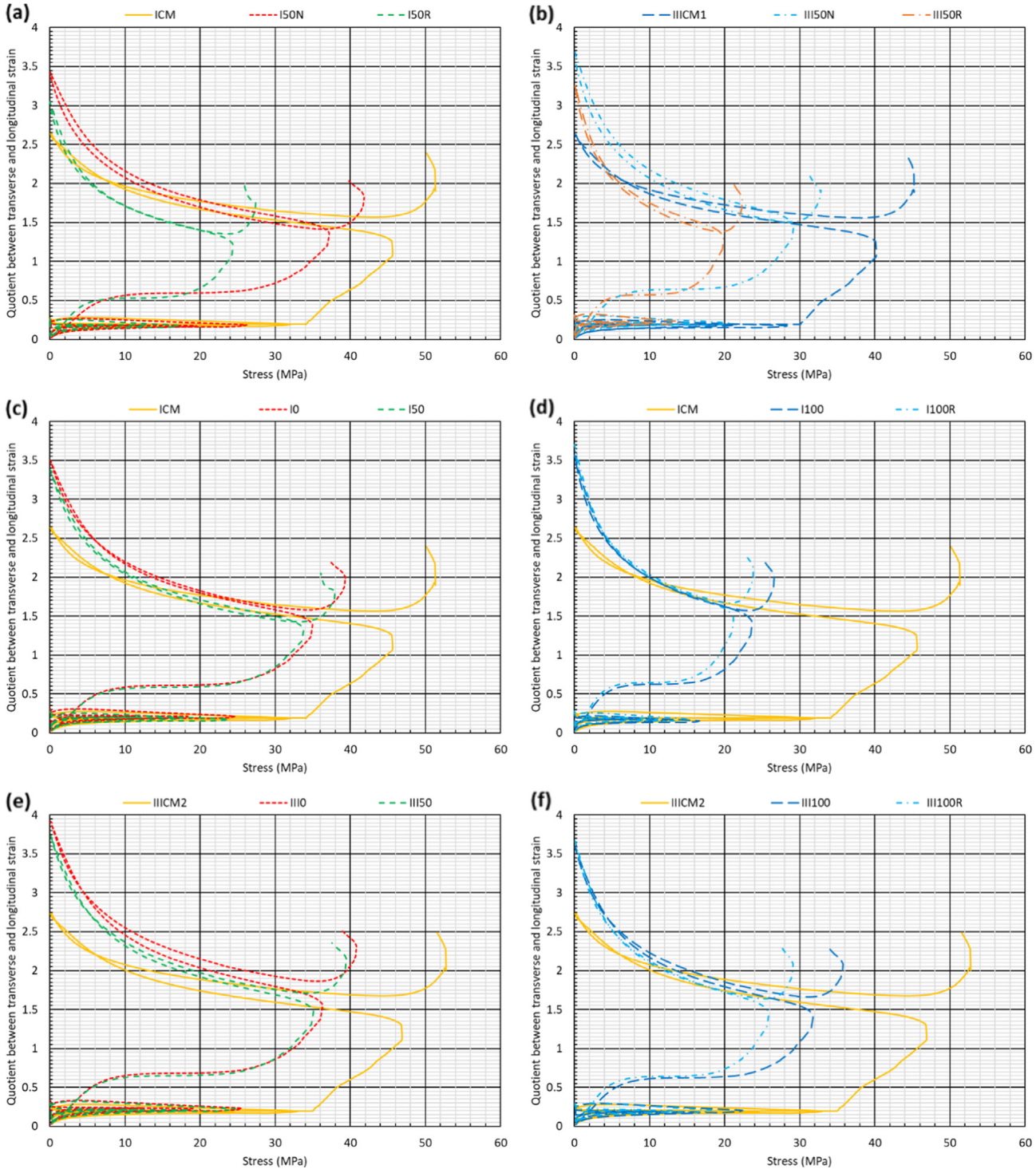

Fig. 13. Relationship between transversal and longitudinal strain (ν-value) in the loading/unloading test: (a, b) batch 1; (c, d) batch 2; (e, f) batch 3.

great importance for the successful application of recycled concrete in real structures and, it still has many research avenues that remain open, such as studying the effect of other contents of coarse RCA, and evaluating the application of other load levels in the loading/unloading test. This study has therefore contributed to understanding the plastic behavior and, especially, the transversal strain patterns of concrete under axial loading.

CRediT authorship contribution statement

Víctor Revilla-Cuesta: Formal analysis, Writing - original draft. **Marta Skaf:** Conceptualization, Methodology, Data curation. **Amaia Santamaría:** Investigation, Validation, Writing - review & editing. **Vanesa Ortega-López:** Writing - review & editing, Supervision, Project administration. **Juan Manuel Manso:** Resources, Funding acquisition.

Declaration of Competing Interest

The authors declare that they have no known competing financial interests or personal relationships that could have appeared to influence the work reported in this paper.

Acknowledgements

This work was supported by the Spanish Ministry MCIU, AEI and ERDF [grant numbers FPU17/03374 and RTI2018-097079-B-C31; 10.13039/501100011033]; the Junta de Castilla y León (Regional Government) and ERDF [grant number UIC-231, BU119P17]; Youth Employment Initiative (JCyL) and ESF [grant number UBU05B_1274]; the University of Burgos [grant number SUCONS, Y135.GI], UPV/EHU (PPGA20/26) and, finally, our thanks also to the Basque Government research group IT1314-19.

References

[1] Y.Y. Lim, K.Z. Kwong, W.Y.H. Liew, R.V. Padilla, C.K. Soh, Parametric study and modeling of PZT based wave propagation technique related to practical issues in monitoring of concrete curing, Constr. Build. Mater. 176 (2018) 519–530, https://doi.org/10.1016/j.conbuildmat.2018.05.074.
[2] R.V. Silva, J. De Brito, R.K. Dhir, The influence of the use of recycled aggregates on the compressive strength of concrete: A review, Europ. J. Environ. Civil Eng. 19 (7) (2015) 825–849, https://doi.org/10.1080/19648189.2014.974831.
[3] EC-2, Eurocode 2: Design of concrete structures. Part 1-1: General rules and rules for buildings, CEN (European Committee for Standardization) (2010).
[4] R.V. Silva, J. de Brito, R.K. Dhir, Fresh-state performance of recycled aggregate concrete: A review, Constr. Build. Mater. 178 (2018) 19–31, https://doi.org/10.1016/j.conbuildmat.2018.05.149.
[5] V. Revilla-Cuesta, M. Skaf, F. Faleschini, J.M. Manso, V. Ortega-López, Self-compacting concrete manufactured with recycled concrete aggregate: An overview, J. Cleaner Prod. 262 (2020) 121362, https://doi.org/10.1016/j.jclepro.2020.121362.
[6] H. Okamura, M. Ouchi, Self-compacting concrete, J. Adv. Concr. Technol. 1 (1) (2003) 5–15, https://doi.org/10.3151/jact.1.5.
[7] M.S. Abo Dhaheer, S. Kulasegaram, B.L. Karihaloo, Simulation of self-compacting concrete flow in the J-ring test using smoothed particle hydrodynamics (SPH), Cem. Concr. Res. 89 (2016) 27–34, https://doi.org/10.1016/j.cemconres.2016.07.016.
[8] A. Santamaría, V. Ortega-López, M. Skaf, J.A. Chica, J.M. Manso, The study of properties and behavior of self compacting concrete containing Electric Arc Furnace Slag (EAFS) as aggregate, Ain Shams Eng. J. 11 (1) (2020) 231–243, https://doi.org/10.1016/j.asej.2019.10.001.
[9] W.S. Alyhya, S. Kulasegaram, B.L. Karihaloo, Simulation of the flow of self-compacting concrete in the V-funnel by SPH, Cem. Concr. Res. 100 (2017) 47–59, https://doi.org/10.1016/j.cemconres.2017.05.021.
[10] N.H. Roslan, M. Ismail, N.H.A. Khalid, B. Muhammad, Properties of concrete containing electric arc furnace steel slag and steel sludge, J. Build. Eng. 28 (2020) 101060, https://doi.org/10.1016/j.jobe.2019.101060.
[11] L. Jin, M. Liu, R. Zhang, X. Du, Cracking of cover concrete due to non-uniform corrosion of corner rebar: A 3D meso-scale study, Constr. Build. Mater. 245 (2020) 118449, https://doi.org/10.1016/j.conbuildmat.2020.118449.
[12] R.V. Silva, J. De Brito, R.K. Dhir, Establishing a relationship between modulus of elasticity and compressive strength of recycled aggregate concrete, J. Cleaner Prod. 112 (2016) 2171–2186, https://doi.org/10.1016/j.jclepro.2015.10.064.
[13] F. Aslani, S. Nejadi, Mechanical characteristics of self-compacting concrete with and without fibres, Mag. Concr. Res. 65 (10) (2013) 608–622, https://doi.org/10.1680/macr.12.00153.
[14] J.T. San-José, J.M. Manso, Fiber-reinforced polymer bars embedded in a resin concrete: Study of both materials and their bond behavior, Polym. Compos. 27 (3) (2006) 315–322, https://doi.org/10.1002/pc.20188.
[15] P. Li, L. Sui, F. Xing, Y. Zhou, Static and cyclic response of low-strength recycled aggregate concrete strengthened using fiber-reinforced polymer, Compos. B Eng. 160 (2019) 37–49, https://doi.org/10.1016/j.compositesb:2018.10.002.
[16] F. Aslani, S. Nejadi, Self-compacting concrete incorporating steel and polypropylene fibers: Compressive and tensile strengths, moduli of elasticity and rupture, compressive stress–strain curve, and energy dissipated under compression, Compos. B Eng. 53 (2013) 121–133, https://doi.org/10.1016/j.compositesb:2013.04.044.
[17] ACI-318-19, Building Code Requeriments for Structural Concrete (2019).
[18] A.L.B. Marinho, C.M. Mol Santos, J.M.F. de Carvalho, J.C. Mendes, G.J. Brigolini, R.A.F. Peixoto, Ladle furnace slag as binder for cement-based composites, J. Mater. Civ. Eng. 29 (11) (2017) 04017207, https://doi.org/10.1061/(ASCE)MT.1943-5533.0002061.
[19] H. Qasrawi, I. Asi, Effect of bitumen grade on hot asphalt mixes properties prepared using recycled coarse concrete aggregate, Constr. Build. Mater. 121 (2016) 18–24, https://doi.org/10.1016/j.conbuildmat.2016.05.101.
[20] M. Pasetto, A. Baliello, G. Giacomello, E. Pasquini, Sustainable solutions for road pavements: A multi-scale characterization of warm mix asphalts containing steel slags, J. Cleaner Prod. 166 (2017) 835–843, https://doi.org/10.1016/j.jclepro.2017.07.212.
[21] L. Lei, H.-K. Chan, Investigation into the molecular design and plasticizing effectiveness of HPEG-based polycarboxylate superplasticizers in alkali-activated slag, Cem. Concr. Res. 136 (2020) 106150, https://doi.org/10.1016/j.cemconres.2020.106150.
[22] H.L. Wu, F. Jin, Y.L. Bo, Y.J. Du, J.X. Zheng, Leaching and microstructural properties of lead contaminated kaolin stabilized by GGBS-MgO in semi-dynamic leaching tests, Constr. Build. Mater. 172 (2018) 626–634, https://doi.org/10.1016/j.conbuildmat.2018.03.164.
[23] M.D.S. Magalhães, F. Faleschini, C. Pellegrino, K. Brunelli, Influence of alkali addition on the setting and mechanical behavior of cement pastes and mortars with electric arc furnace dust, Constr. Build. Mater. 214 (2019) 413–419, https://doi.org/10.1016/j.conbuildmat.2019.04.141.
[24] J.A. Fuente-Alonso, V. Ortega-López, M. Skaf, Á. Aragón, J.T. San-José, Performance of fiber-reinforced EAF slag concrete for use in pavements, Constr. Build. Mater. 149 (2017) 629–638, https://doi.org/10.1016/j.conbuildmat.2017.05.174.
[25] M. Etxeberria, A. Gonzalez-Corominas, P. Pardo, Influence of seawater and blast furnace cement employment on recycled aggregate concretes' properties, Constr. Build. Mater. 115 (2016) 496–505, https://doi.org/10.1016/j.conbuildmat.2016.04.064.
[26] A.-L. Beaucour, P. Pliya, F. Faleschini, R. Njinwoua, C. Pellegrino, A. Noumowé, Influence of elevated temperature on properties of radiation shielding concrete with electric arc furnace slag as coarse aggregate, Constr. Build. Mater. 256 (2020) 119385, https://doi.org/10.1016/j.conbuildmat.2020.119385.
[27] V. Revilla-Cuesta, M. Skaf, J.A. Chica, J.A. Fuente-Alonso, V. Ortega-López, Thermal deformability of recycled self-compacting concrete under cyclical temperature variations, Mater. Lett. 278 (2020) 128417, https://doi.org/10.1016/j.matlet.2020.128417.
[28] A.R. Khan, S. Fareed, M.S. Khan, Use of recycled concrete aggregates in structural concrete, Sustain. Constr. Mater. Technol. 2 (2019).
[29] F. Fiol, C. Thomas, C. Muñoz, V. Ortega-López, J.M. Manso, The influence of recycled aggregates from precast elements on the mechanical properties of structural self-compacting concrete, Constr. Build. Mater. 182 (2018) 309–323, https://doi.org/10.1016/j.conbuildmat.2018.06.132.
[30] I. González-Taboada, B. González-Fonteboa, J.L. Pérez-Ordóñez, J. Eiras-López, Prediction of self-compacting recycled concrete mechanical properties using vibrated recycled concrete experience, Constr. Build. Mater. 131 (2017) 641–654, https://doi.org/10.1016/j.conbuildmat.2016.11.112.
[31] A.S. Brand, A.N. Amirkhanian, J.R. Roesler, Flexural capacity of full-depth and two-lift concrete slabs with recycled aggregates, Transp. Res. Rec. 2456 (1) (2014) 64–72, https://doi.org/10.3141/2456-07.
[32] K.H. Yang, Y.H. Hwang, Y. Lee, J.H. Mun, Feasibility test and evaluation models to develop sustainable insulation concrete using foam and bottom ash aggregates, Constr. Build. Mater. 225 (2019) 620–632, https://doi.org/10.1016/j.conbuildmat.2019.07.130.
[33] C. Wang, J. Xiao, Evaluation of the stress-strain behavior of confined recycled aggregate concrete under monotonic dynamic loadings, Cem. Concr. Compos. 87 (2018) 149–163, https://doi.org/10.1016/j.cemconcomp.2017.12.012.
[34] Z. Tang, W. Li, V.W.Y. Tam, Z. Luo, Investigation on dynamic mechanical properties of fly ash/slag-based geopolymeric recycled aggregate concrete, Compos. B Eng. 185 (2020) 107776, https://doi.org/10.1016/j.compositesb:2020.107776.
[35] H. Zhao, F. Liu, H. Yang, Residual compressive response of concrete produced with both coarse and fine recycled concrete aggregates after thermal exposure, Constr. Build. Mater. 244 (2020) 118397, https://doi.org/10.1016/j.conbuildmat.2020.118397.
[36] S. Luo, S. Ye, J. Xiao, J. Zheng, Y. Zhu, Carbonated recycled coarse aggregate and uniaxial compressive stress-strain relation of recycled aggregate concrete, Constr. Build. Mater. 188 (2018) 956–965, https://doi.org/10.1016/j.conbuildmat.2018.08.159.
[37] S.M.S. Kazmi, M.J. Munir, Y.F. Wu, I. Patnaikuni, Y. Zhou, F. Xing, Axial stress-strain behavior of macro-synthetic fiber reinforced recycled aggregate concrete, Cem. Concr. Compos. 97 (2019) 341–356, https://doi.org/10.1016/j.cemconcomp.2019.01.005.
[38] F. Faleschini, M.A. Zanini, L. Hofer, K. Toska, D. De Domenico, C. Pellegrino, Confinement of reinforced concrete columns with glass fiber reinforced cementitious matrix jackets, Eng. Struct. 218 (2020) 110847, https://doi.org/10.1016/j.engstruct.2020.110847.
[39] Z. Xiong, Q. Cai, F. Liu, L. Li, Y. Long, Dynamic performance of RAC-filled double-skin tubular columns subjected to cyclic axial compression, Constr. Build. Mater. 248 (2020) 118665, https://doi.org/10.1016/j.conbuildmat.2020.118665.
[40] J.M. Lee, Y.J. Lee, Y.J. Jung, J.H. Park, B.S. Lee, K.H. Kim, Ductile capacity of reinforced concrete columns with electric arc furnace oxidizing slag aggregate, Constr. Build. Mater. 162 (2018) 781–793, https://doi.org/10.1016/j.conbuildmat.2017.12.045.
[41] S.W. Kim, Y.S. Kim, J.M. Lee, K.H. Kim, Structural performance of spirally confined concrete with EAF oxidising slag aggregate, Europ. J. Environmen. Civil Eng. 17 (8) (2013) 654–674, https://doi.org/10.1080/19648189.2013.810178.

[42] A. Gholampour, T. Ozbakkaloglu, O. Gencel, T.D. Ngo, Concretes containing waste-based materials under active confinement, Constr. Build. Mater. 270 (2021) 121465, https://doi.org/10.1016/j.conbuildmat.2020.121465.
[43] Y. Chen, Z. Chen, J. Xu, E.M. Lui, B.o. Wu, Performance evaluation of recycled aggregate concrete under multiaxial compression, Constr. Build. Mater. 229 (2019) 116935, https://doi.org/10.1016/j.conbuildmat.2019.116935.
[44] X. Hu, Q. Lu, Z. Xu, W. Zhang, S. Cheng, Compressive stress-strain relation of recycled aggregate concrete under cyclic loading, Constr. Build. Mater. 193 (2018) 72–83, https://doi.org/10.1016/j.conbuildmat.2018.10.137.
[45] EN-Euronorm, Rue de stassart, 36. Belgium-1050 Brussels, European Committee for Standardization.
[46] H. Salehi, M. Mazloom, Opposite effects of ground granulated blast-furnace slag and silica fume on the fracture behavior of self-compacting lightweight concrete, Constr. Build. Mater. 222 (2019) 622–632, https://doi.org/10.1016/j.conbuildmat.2019.06.183.
[47] V. Revilla-Cuesta, V. Ortega-López, M. Skaf, J.M. Manso, Effect of fine recycled concrete aggregate on the mechanical behavior of self-compacting concrete, Constr. Build. Mater. 263 (2020) 120671, https://doi.org/10.1016/j.conbuildmat.2020.120671.
[48] S. Santos, P.R. da Silva, J. de Brito, Self-compacting concrete with recycled aggregates – A literature review, J. Build. Eng. 22 (2019) 349–371, https://doi.org/10.1016/j.jobe.2019.01.001.
[49] M.C.S. Nepomuceno, L.A. Pereira-de-Oliveira, S.M.R. Lopes, Methodology for the mix design of self-compacting concrete using different mineral additions in binary blends of powders, Constr. Build. Mater. 64 (2014) 82–94, https://doi.org/10.1016/j.conbuildmat.2014.04.021.
[50] A. Santamaría, A. Orbe, M.M. Losañez, M. Skaf, V. Ortega-Lopez, J.J. González, Self-compacting concrete incorporating electric arc-furnace steelmaking slag as aggregate, Mater. Des. 115 (2017) 179–193, https://doi.org/10.1016/j.matdes.2016.11.048.
[51] V. Revilla-Cuesta, M. Skaf, R. Serrano-López, V. Ortega-López, Models for compressive strength estimation through non-destructive testing of highly self-compacting concrete containing recycled concrete aggregate and slag-based binder, Constr. Build. Mater. 280 (2021) 122454, https://doi.org/10.1016/j.conbuildmat.2021.122454.
[52] D. Pedro, J. de Brito, L. Evangelista, Mechanical characterization of high performance concrete prepared with recycled aggregates and silica fume from precast industry, J. Cleaner Prod. 164 (2017) 939–949, https://doi.org/10.1016/j.jclepro.2017.06.249.
[53] Annual Book of ASTM Standards, ASTM International, West Conshohocken, 19429-2959. PA, USA, 2008.
[54] M. Behera, S.K. Bhattacharyya, A.K. Minocha, R. Deoliya, S. Maiti, Recycled aggregate from C&D waste & its use in concrete - A breakthrough towards sustainability in construction sector: A review, Constr. Build. Mater. 68 (2014) 501–516, https://doi.org/10.1016/j.conbuildmat.2014.07.003.
[55] CEB-FIP, Model Code 2010 (Volumes 1 and 2) (2012).
[56] ANSI/AISC-360-16, Specification for Structural Steel Buildings (2016)